Oligodendrocyte Lineage and Subventricular Zone Response to Traumatic Axonal Injury in the Corpus Callosum

Genevieve M. Sullivan, BS, Amanda J. Mierzwa, PhD, Naruchorn Kijpaisalratana, MD,
*Haiying Tang, PhD, Yong Wang, PhD, Sheng-Kwei Song, PhD, Reed Selwyn, PhD,
and Regina C. Armstrong, PhD

Abstract

Traumatic brain injury frequently causes traumatic axonal injury (TAI) in white matter tracts. Experimental TAI in the corpus callosum of adult mice was used to examine the effects on oligodendrocyte lineage cells and myelin in conjunction with neuroimaging. The injury targeted the corpus callosum over the subventricular zone, a source of neural stem/progenitor cells. Traumatic axonal injury was produced in the rostral body of the corpus callosum by impact onto the skull at the bregma. During the first week after injury, magnetic resonance diffusion tensor imaging showed that axial diffusivity decreased in the corpus callosum and that corresponding regions exhibited significant axon damage accompanied by hypertrophic microglia and reactive astrocytes. Oligodendrocyte progenitor proliferation increased in the subventricular zone and corpus callosum. Oligodendrocytes in the corpus callosum shifted toward upregulation of myelin gene transcription. *Plp/CreER^T:R26IAP* reporter mice showed normal reporter labeling of myelin sheaths 0 to 2 days after injury but labeling was increased between 2 and 7 days after injury. Electron microscopy revealed axon degeneration, demyelination, and redundant myelin figures. These findings expand the cell types and responses to white matter injuries that inform diffusion tensor imaging evaluation and identify pivotal white matter changes after TAI that may affect axon vulnerability vs. recovery after brain injury.

INTRODUCTION

Traumatic brain injury (TBI) is experienced by millions of people worldwide (1). White matter tracts, particularly the corpus callosum (CC), are a common site of traumatic axonal injury (TAI) resulting from high strain forces, including those experienced in contact sports-associated TBI (2–6). Traumatic brain injury with TAI is associated with neuroimaging indicators of white matter abnormalities that can be detected by computed tomography in patients with severe TBI with diffuse axonal injury; they are, however, more difficult to detect in mild-moderate injuries (3, 4, 7). Consequently, additional approaches are being developed with magnetic resonance imaging, such as diffusion tensor imaging (DTI) (3, 4, 7–9). While patients with mild-moderate TBI often recover substantially during a subacute period, 1 or more symptoms may be experienced chronically, even as a result of a single TBI or without positive findings on a head computed tomography (1, 10). Therefore, improved assessment tools are needed to detect the pathologic features that are predictive of a worse outcome. It is particularly important to understand the cellular and molecular changes that can facilitate endogenous repair processes and guide the development of interventions to improve recovery among those patients identified as being at risk of poor recovery. Currently, there are no effective treatments for TAI (6).

Traumatic axonal injury is accompanied by complex reactions among glial populations in white matter tracts. Damage to myelin can be a major component of white matter injury. Indeed, oligodendrocyte cell loss has been demonstrated within the first week after a moderate fluid percussion injury in rats (11) and in acute and chronic human TBI (12). It is unclear to what extent different forms of TBI result in demyelination along viable axons versus myelin sheath degeneration subsequent to axonal transection. Remyelination of denuded axons, which can promote functional recovery and prevent further axonal damage, occurs within the first month after trauma from experimental spinal cord injury (13). Further studies are needed to examine the capacity for remyelination after white matter damage from TBI. In multiple sclerosis (MS) and models of experimental demyelination of the CC, oligodendrocyte progenitor (OP) cells persisting in adult white matter or generated from the subventricular zone (SVZ), proliferate

and differentiate into myelin-forming oligodendrocytes to accomplish remyelination (14–16). Multiple factors in injured tissues can impair this spontaneous remyelination capacity (17). For example, activated microglia must clear myelin debris for remyelination to proceed (18). Reactive microglia have been observed in the CC in human TBI cases and may contribute to chronic degenerative changes even a year or more after a single TBI (19). Experimental models have shown that, in response to diverse forms of CNS trauma, reactive astrocytes can produce growth factors that support axon integrity and OP proliferation but can also form glial scars that impair regeneration of transected axons (20). Thus, to understand the progression of damage versus repair in the white matter after TBI, the components cellular responses to TAI need to be characterized.

The current study was the first to examine oligodendrocyte lineage changes, from the endogenous neural stem/progenitor cell response through myelination, after experimental TAI in white matter in conjunction with neuroimaging. Whereas rodent studies of axonal damage in the CC have focused on the caudal CC overlying the hippocampus to examine memory impairment and regenerative responses from the subgranular zone, the current study examined TAI focused more rostrally to facilitate analysis of the potential for white matter repair from OP cells within the CC and neural stem cells in the adjacent SVZ, the largest germinal zone in the mammalian CNS. Ex vivo and in vivo DTI were combined with postimaging histologic and immunohistochemical analyses. The extent of TAI was quantified along with changes in myelination. Reactive stages of microglia and astrocytes were characterized as potentially contributing to the interpretation of DTI changes and to regulatory signaling in the lesion environment. Proliferation of the OP cells in the SVZ and CC was monitored using 5-bromo-2'-deoxyuridine (BrdU) pulse-chase labeling. In situ hybridization for myelin proteolipid protein (PLP) enabled identification of oligodendrocytes and comparison of transcriptional activation of this major myelin gene. The *Plp* promoter was also exploited in *Plp/CreER^T* mice crossed to the *R26IAP* reporter line for conditional inducible expression of alkaline phosphatase (AP) in oligodendrocytes. After tamoxifen administration, only oligodendrocytes with intact processes can label myelin sheaths with AP, which enables screening for potential disruption of the oligodendrocyte-myelin unit after injury. Corpus callosum regions of interest were further examined by electron microscopy to provide ultrastructural correlation of the pathologic findings with the corresponding DTI values and cellular responses. This combination of approaches strengthens the interpretation of DTI findings and identifies potential regenerative changes ongoing in the white matter after TAI.

MATERIALS AND METHODS

All procedures were performed with 8- to 10-week-old male C57BL/6 mice (Jackson Laboratories, Bar Harbor, ME) or *Plp/CreER^T:R26IAP* mice (detailed below). Mice were housed singly or in pairs on site in the animal facility according to the guidelines of the National Institutes of Health and the Institutional Animal Care and Use Committee of the Uniformed Services University of the Health Sciences.

Traumatic Axonal Injury

The method to induce TAI in mice was modified from Creed et al (21), to involve the rostral body of the CC adjacent to the SVZ and increase head stabilization. An Impact One Stereotaxic Impactor device was used to produce a controlled impact to the skull. Mice were placed in the stereotaxic frame and secured with ear bars that were inverted and covered with rubber stoppers. Isoflurane was administered continuously at 2% via a nose cone until immediately after impact. A 3-mm-diameter flat impact tip was centered over the bregma and set to an impact depth of either 1.0 mm (n = 14), 1.5 mm (n = 29), or 2.0 mm (n = 10) from the skull surface; an impact velocity of 5 m/s; and a dwell time of 100 ms. With these settings for the 1.5 -m depth, video analysis of the impact velocity and depth verified an average impact velocity of 4.7 m/s and depth of 1.7 mm. Sham mice (n = 12) received anesthesia as well as an incision to the scalp. Naïve mice (n = 11) did not receive anesthesia or surgery.

Ex Vivo Cross-sectional DTI

For ex vivo DTI, concussive brain injury (n = 5) and sham (n = 5) mice were perfused with 4% paraformaldehyde at 3 days after injury and brains were postfixed overnight in fixative. Brains were kept in phosphate-buffered saline at 4°C for approximately 2 weeks before scanning. Images were acquired using a 4.7T Agilent DirectDrive small-animal MRI system (Agilent Technologies, Santa Clara, CA) equipped with Magnex/Agilent HD imaging gradient coil (Magnex/Agilent, Oxford, UK), with pulse gradient strength up to 58 G/cm and a gradient rise time of 295 μs or less. Coronal images were acquired throughout the rostral-caudal extent of the CC and were registered according to the anatomical position at which the anterior commissure crossed the midline. A multiple-echo spin-echo imaging sequence was used to acquire diffusion-weighted images with the acquisition parameters: repetition time (TR) = 800 ms, echo time (TE) = 33.2 ms, data matrix = 256 × 256, field of view = 22 × 22 mm^2, number of slices = 8, slice thickness = 0.5 mm, 3 repetitions, and total scanning time = 17 hours. The diffusion encoding scheme used 99 diffusion-weighted directions selected as prescribed in diffusion spectrum imaging where the position vectors are the entire grid points (q_x, q_y, q_z) over the 3-dimensional q-space under the relationship that $(q_x^2 + q_y^2 + q_z^2) \leq r^2$ (sum of square ≤ square of r), where $r = 3$ for the current measurements (22–24): time between diffusion gradients (Δ) = 16 ms, diffusion gradient duration (Δ) = 5 ms, and max b value = 3,200 s/mm^2. As previously reported (25), fractional anisotropy (FA), axial ($\lambda_\parallel$), and radial diffusivity ($\lambda_\perp$) were derived using software written in MATLAB (MathWorks, Natick, MA) on a pixel-by-pixel basis. The CC from the midline laterally to the point of ventral curvature in the external capsule was manually defined as region of interest on the color-coded relative anisotropy maps using National Institutes of Health ImageJ, as in our previous study (26).

In Vivo DTI Longitudinal Study

An in vivo longitudinal study was carried out on an additional cohort of 5 mice with DTI conducted at −1 (baseline), 1, 3, and 7 days after injury. Images were acquired

at each time point using a 7 T/20 cm BioSpec system (Bruker NMR, Inc., Billerica, MA). Accelerated T2-weighted images were acquired using a 2-dimensional rapid acquisition and relaxation enhancement (RARE) protocol with TR = 12,000; TE = 7.5 ms; effective echo times = 15, 45, 75, 105 ms; NA = 4; RARE factor = 4; matrix = 128 × 128 × 50; field of view = 12.8 mm × 12.8 mm; number of slices = 50; slice thickness = 0.25 mm; slice gap = 0.05 mm/interlaced. T2 images were processed using VivoQuantTM (inviCRO, Boston, MA). Spin-echo multishot echo-planar imaging sequence was used to acquire diffusion-weighted images with the following acquisition parameters: echo-planar imaging segments = 8, TR = 3,000 ms, TE = 20 ms, $\Delta = 9$ ms, $\delta = 3.6$ ms, max b value = 1,000 s/mm^2, diffusion directions = 30, data matrix = 128 × 128, field of view = 12.8 × 12.8 mm^2, number of slices = 12, slice thickness = 0.5 mm, and total scan time = 40 minutes. In vivo DTI data were analyzed using TORTOISE software (27).

Histopathology and Immunohistochemistry

Mice were perfused with paraformaldehyde using 3% for frozen section preparations and 4% for paraffin embedding. Brains were further postfixed by immersion overnight. Seven-micrometer-thick paraffin-embedded sections were stained with hematoxylin and eosin for general analysis of cellular organization and Luxol fast blue with periodic acid–Schiff to detect myelin and activation of macrophages/microglia, respectively. Frozen 14-μm coronal cryosections were used for Prussian blue stain for hemosiderin combined with pararosaniline nuclear stain (Sigma, St. Louis, MO).

Cryosections (4 μm) were immunostained with the following primary antibodies: rabbit polyclonal β-amyloid precursor protein (βAPP, 1:100; Life Technologies, Grand Island, NY), rabbit polyclonal NG2 (1:500; a gift from Dr. William Stallcup), rabbit polyclonal glial fibrillary acidic protein (GFAP, 1:500; DAKO, Carpinteria, CA), mouse monoclonal myelin oligodendrocyte glycoprotein (MOG [28]), and rat monoclonal CD11b (1:100; AbCam, Cambridge, MA). Secondary antibodies included donkey anti-rabbit IgG F(ab')2 conjugated with Cy3 (Jackson ImmunoResearch, West Grove, PA) to detect βAPP or NG2, goat anti-rat IgG conjugated with Alexa Fluor 555 (1:200; Life Technologies) to detect CD11b, donkey anti-mouse IgG conjugated with Cy3 (Jackson ImmunoResearch) to detect MOG, and goat anti-rabbit IgG conjugated with Alexa Fluor 488 (1:200; Life Technologies) to detect GFAP. Sections were counterstained with DAPI (Sigma Aldrich) before mounting with Vectashield (Vector Laboratories, Burlingame, CA). NG2/BrdU and Ki67/GFAP combined immunostained tissues were quantified by manually counting cells immunolabeled in each fluorescent channel and using Spot Advanced (Sterling Heights, MI) to measure the area counted within the CC and SVZ based on DAPI nuclear staining. Myelination (MOG) was estimated based on pixel intensity values to determine the immunolabeled pixels above background levels within the CC using Metamorph (Molecular Devices, Downington, PA), as previously detailed (29). Astrogliosis (GFAP) and microglia activation (CD11b) were also quantified by similar thresholding so that pixels above background level correspond to the immunostained area to take into account changes in morphology and/or expression

that can accompany reactive gliosis. Axons were identified as damaged based on the presence of dense βAPP immunoreactivity either appearing as large single end bulbs or as multiple swellings along a longitudinal axonal profile (30, 31). Quantification of immunohistochemistry after injury was compared to sham or naive depending on the cross-sectional or longitudinal neuroimaging study design. In the cross-sectional study, the ex vivo DTI data are compared between sham and TBI with both tissues analyzed after imaging. In the longitudinal study, the in vivo postinjury DTI data are compared to baseline so that additional naive mice are the appropriate comparison.

In Situ Hybridization

In situ hybridization was performed using a riboprobe to hybridize to PLP mRNA, as previously described (27, 28). After hybridization, labeling was detected with AP-conjugated sheep anti-digoxigenin and reaction with substrate solution (nitroblue tetrazolium chloride/5-bromo-4-chloro-3-indolyl-phosphate [NBT/BCIP]; Dako). The majority of oligodendrocytes of the normal adult CC can be identified by the presence of PLP mRNA transcripts in the perinuclear cytoplasm. A minority of oligodendrocytes in the normal adult CC exhibit a higher level of PLP expression creating a darker substrate reaction that fills the cell body and often extends into the processes. In conditions of remyelination, high PLP-expressing cells increase in frequency and in substrate intensity (27, 28).

Analysis of Cell Proliferation

Cells actively dividing at the time of perfusion were identified by immunostaining for Ki67 (rat monoclonal, 1:50; DAKO), which was detected with goat anti-rat IgG conjugated with Alexa Fluor 555 (1:200; Life Technologies). In addition, a pulse-chase labeling protocol was used to monitor the proliferative response of endogenous neural stem and progenitor cells throughout the first week after injury. Mice received an intraperitoneal injection with 200 mg/kg of BrdU (Sigma Aldrich) at 24 and 22 hours before concussive brain injury or sham surgery, and tissue was collected at 1, 3, or 7 days after injury. Tissue sections were processed for immunohistochemistry as above with the addition of digestion with proteinase K (Sigma Aldrich) followed by treatment with 2N HCl before the addition of blocking solution. Sections were incubated overnight with anti-BrdU antibody conjugated to fluorescein (Roche Diagnostics, Indianapolis, IN).

Plp/CreER^T:R26IAP Mice

Transgenic *Plp/CreER^T:R26IAP* mice were generated from crosses of the *Plp/CreER^T* driver line to the *R26IAP* reporter line. Mice of both genders were divided into each cohort. In *Plp/CreER^T* mice, the *Plp* promoter drives conditional expression in oligodendrocyte lineage cells of Cre recombinase fused to a mutated estrogen receptor (32). The *R26IAP* mice constitutively express a floxed inverted second exon of the gene for the membrane-associated form of human AP (33). In *Plp/CreER^T:R26IAP* mice, tamoxifen induces heritable AP synthesis in oligodendrocytes, with corresponding AP accumulation in myelin membranes (34). Tamoxifen was
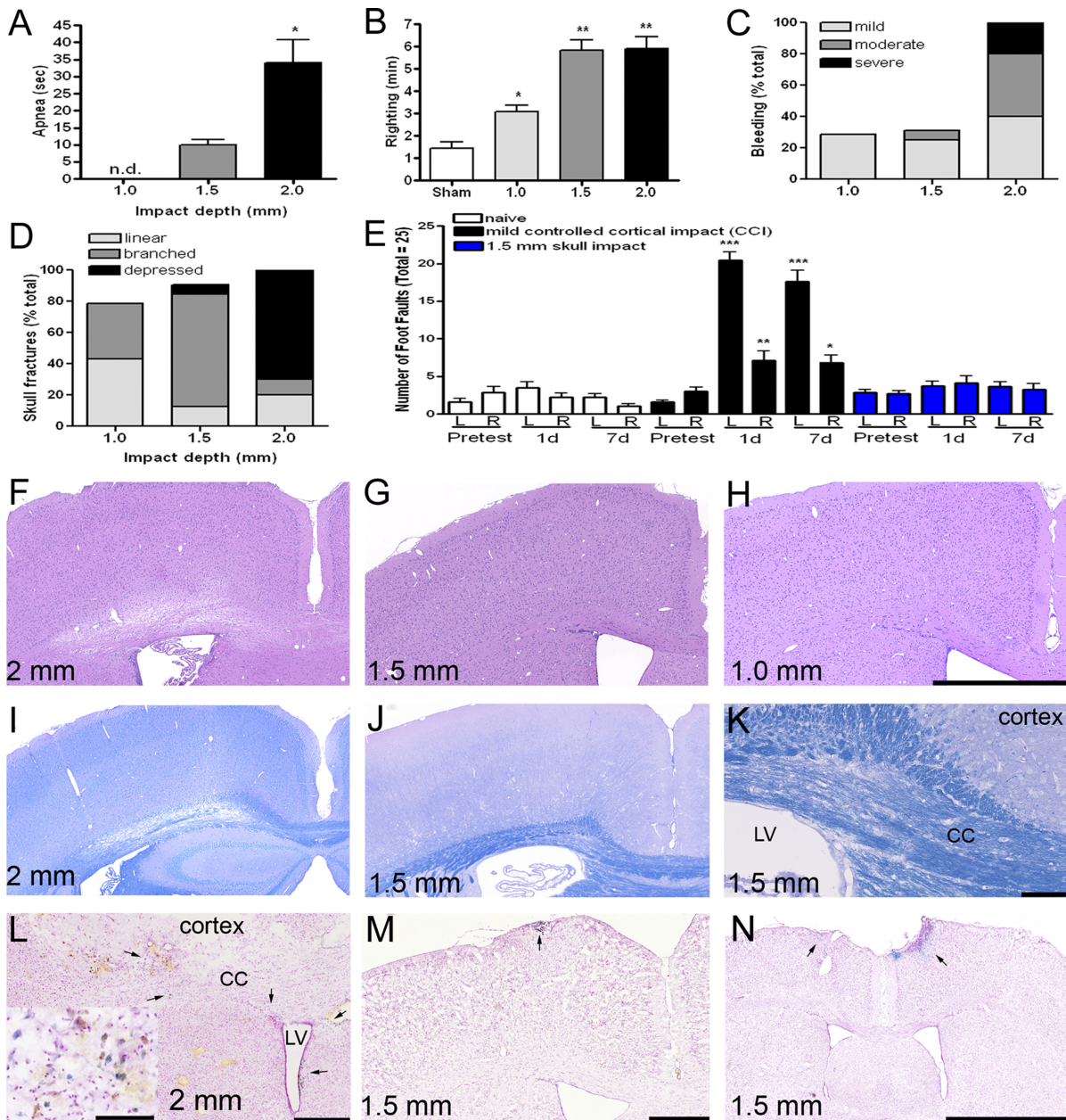
FIGURE 1. Postsurgical response and histopathology vary with impact depth. **(A–E)** Increasing the depth of impact increased the duration of apnea **(A)**, delayed the righting response **(B)**, produced more severe bleeding **(C)**, increased the severity of skull fractures **(D)** (1.0 mm, n = 14; 1.5 mm, n = 29; 2.0 mm, n = 9; sham, n = 7). **(E)** Behavioral testing indicated that the 1.5-mm depth did not produce a marked cortical injury based on comparison to a positive control for test validity, which was a mild controlled cortical impact (CCI). CCI involved a craniotomy and cortical contusion over the right sensorimotor cortex at the same coronal level. The number of foot faults was increased in the beam walk test only after CCI (*, $p < 0.05$; **, $p < 0.01$; ***, $p < 0.001$; naive, n = 11; CCI, n = 21; 1.5-mm skull impact, n = 11). **(F–N)** Histopathologic differences based on impact depth are evident in coronal sections with hematoxylin and eosin staining of cytoarchitecture **(F–H)**, Luxol fast blue staining of myelin **(I–K)**, and Prussian blue detection of hemosiderin **(L–N)**. Depths of impact setting are indicated for mice examined at 3 days **(F–M)** or 1 week **(N)** after injury. The extensive tissue destruction associated with the 2-mm-impact depth at the level of impact **(F)** extended caudally **(I)** as well as rostrally **(L)** and included extravasation of blood cells (brown), and hemosiderin laden macrophages (L, blue cells; arrows; inset shows enlargement of area near upper arrow) within the cerebral cortex, corpus callosum (CC), and subventricular zone (SVZ) adjacent to the lateral ventricle (LV). The 1.5-mm depth **(G, J, M)** resulted in less overt tissue destruction with reduced myelin staining in the CC over the LV **(J**, with higher magnification shown in **K)**. The 1.5-mm depth produced areas with hemosiderin in the superficial cortex **(M–N**, blue cells; arrows**)**. The 1.0-mm impact did not produce changes detected by hematoxylin and eosin **(H)** or the other histologic techniques examined (data not shown). Scale bars = **(F–J**, shown in **H)** 1 mm; **(K)** 100 μm; **(L–M)** 0.5 mm; **(L insert)** 100 μm; **(N)** 2 mm. n.d. = not detected.

administered by oral gavage on 2 consecutive days (10 mg/d). The primary injury stage of 0 to 2 days after injury was examined with tamoxifen administered on Day 0 (2 hours before sham surgery or 1.5 mm impact) and on Day 1 (24 hours after injury) followed by perfusion on Day 2 after surgery. For analysis of a secondary injury stage between 2 and 7 days after
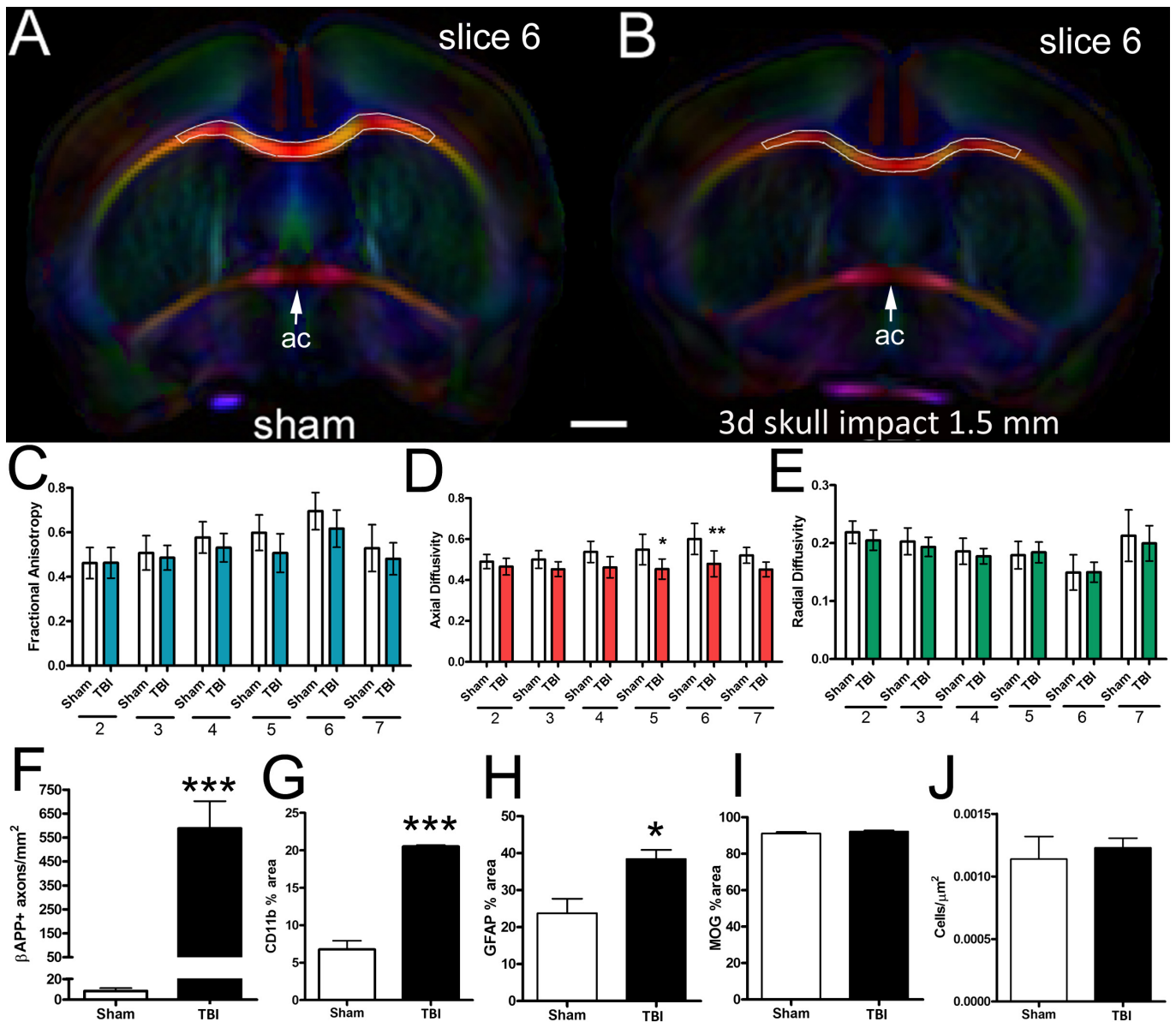

FIGURE 2. Cross-sectional ex vivo diffusion tensor imaging (DTI) with postimaging tissue analysis. **(A, B)** Color-encoded fractional anisotropy (FA) maps from ex vivo DTI of brains at 3 days after sham **(A)** or 1.5-mm impact **(B)**. Coronal slices show the level of the anterior commissure (ac) midline crossing, which corresponds with the coronal level of impact to the skull at the bregma. The color reflects the fiber orientation within the white matter tracts (red = medial-lateral; green = superior-inferior; blue = anterior-posterior). The corpus callosum region of interest is outlined in white. Scale bar = 1 mm. **(C–E)** Comparison across 0.5-mm coronal slices for values of FA **(C)** and the underlying components of axial **(D)** and radial **(E)** diffusivity. Data show slices throughout the body of the corpus callosum (2 = caudal; 6 = ac; 7 = rostral) at 3 days after sham surgery or concussive brain injury (CBI). A significant decrease in axial diffusivity was observed in Slices 5 and 6 of mice with TBI versus sham. *, $p < 0.05$ and **, $p < 0.01$ for injury (n = 5) versus sham (n = 5) for each slice based on 2-way analysis of variance. **(F–J)** Quantification of axon damage **(F**, β-amyloid precursor protein [βAPP] immunolabeling**)**, microglia/macrophage activation **(G**, CD11b immunolabeling**)**, astrogliosis **(H**, glial fibrillary acidic protein [GFAP] immunolabeling**)**, myelination **(I**, MOG, myelin oligodendrocyte glycoprotein immunolabeling**)**, and cellularity **(J**, DAPI nuclear stain**)** in the corpus callosum at coronal levels within Slices 5 and 6 after ex vivo magnetic resonance imaging. Significant increases in axon damage **(F)**, microglia/macrophage activation **(G)**, and astrogliosis **(H)** are evident without changes in myelination **(I)** or cellular density **(J)**. ***, $p < 0.0001$; *, $p < 0.05$ in TBI (n = 5) versus sham (n = 5). Values shown are mean ± SD.

injury, tamoxifen was administered on Days 2 and 3 after surgery (sham or 1.5 mm impact) followed by perfusion on Day 7 after surgery. Coronal tissue sections (14 μm) were incubated in phosphate-buffered saline for heat inactivation of endogenous AP activity (69°C for 90 minutes) and reacted with NBT/BCIP substrate followed by methyl green nuclear counterstain (Vector Laboratories). The intensity of the AP substrate reaction within the CC was quantified using Metamorph to measure the area of pixels within the range of low, medium, or high intensity levels. Pixel intensities for each level were distinguished and thresholded based on pseudocolor boundaries using the LUT histogram. Levels were set relative the overall AP reaction in the tissue, which can be compared between sham and injured mice but not between the 2 different time periods due to different lengths of time after tamoxifen administration. The AP intensity index was calculated as the sum of the pixel number in each area multiplied by a weighting factor based on intensity, i.e., index = (low × 1) + (medium × 2) + (high × 3). Alkaline phosphatase reaction was not detected in tissue sections from mice administered vehicle instead of tamoxifen or in mice with the *R26IAP* allele without *Plp/CreER^T* allele (data not shown).

Electron Microscopy

Mice were perfused with 4% paraformaldehyde. Brains were extracted and postfixed in 4% paraformaldehyde at 4°C overnight. Sagittal and coronal vibratome sections 0 μm)

were cut and placed into 2.5% glutaraldehyde in 0.1 mol/L phosphate buffer at 4°C overnight and then processed for osmication and plastic embedding. Ultrathin sections were collected on formvar-coated copper slot grids and poststained with 2% uranyl acetate followed by Reynolds lead citrate. Digital images were acquired on a JEM-1011transmission electron microscope (JEOL, Peabody, MA) and a XR50 camera (Advanced Microscopy Techniques, Woburn, MA). Demyelinated axons were identified as having undetectable compact myelin when photographed at ×5,000 magnification. Quantification of demyelinated axons excluded axons smaller than 0.3 μm in diameter owing to overlap with the overall mean diameter of unmyelinated axons being 0.25 ± 0.01 μm in the mouse CC (35). Demyelinated axons, degenerated axons, and redundant myelin figures were manually counted in sagittal images of 6 areas (875 μm²/area; 3 areas per grid) of the CC per mouse with at least 3 mice per condition.

Behavioral Assessment

A beam walk test was used to evaluate individual limb function (36). Mice were trained to walk on a 6-mm-wide beam 1 day before injury. Each animal was given 1 trial per test period that consisted of walking the length of the beam 3 times before data collection for the initial time point. The number of foot faults accrued over 50 steps was counted for each hind limb.
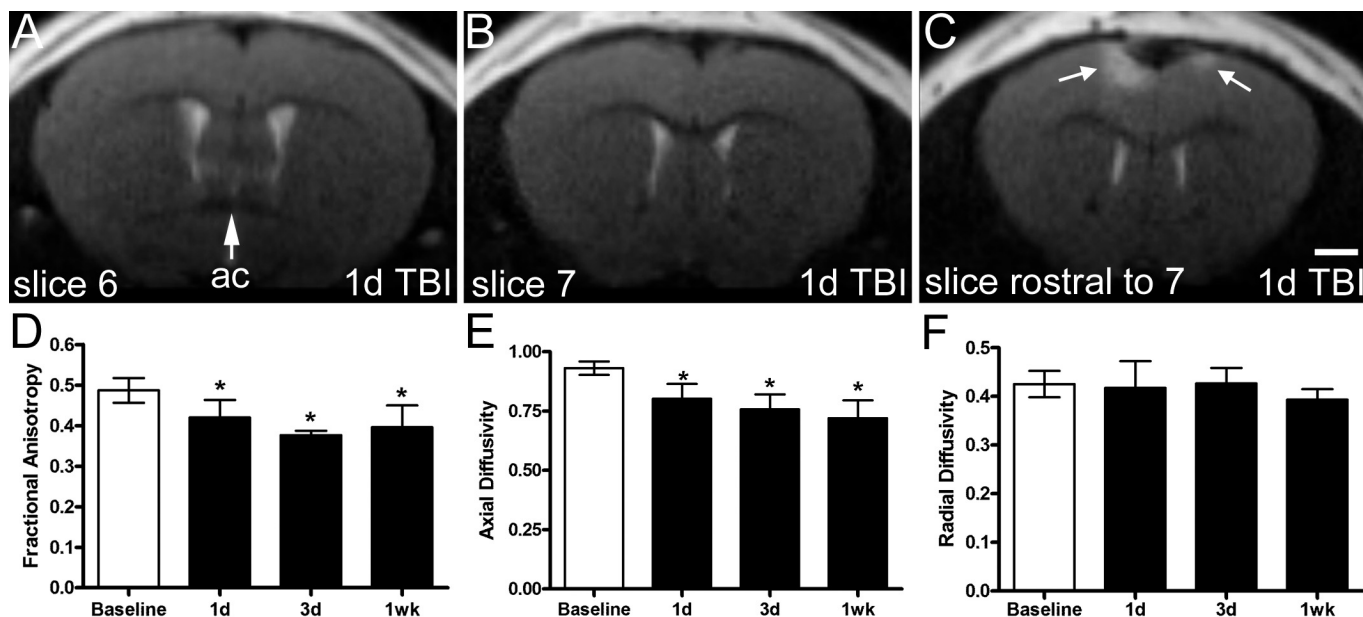

FIGURE 3. Longitudinal in vivo magnetic resonance imaging (MRI) of the cerebral cortex and corpus callosum after the 1.5-mm skull impact. A longitudinal cohort (n = 5 mice) was scanned for baseline measurements on the day before traumatic brain injury (TBI) with repeat scans after injury after 1 day, 3 days, and 1 week. **(A–C)** T2-weighted imaging at the coronal level corresponding to the impact site **(A**; ac = midline crossing of the anterior commissure; Slice 6**)** and at more rostral levels within the body of the corpus callosum **(B**, Slice 7**)** and further rostral **(C**, rostral to scanned region**)**. Areas of T2 signal hyperintensity are present in the superficial cortex in **C** (arrows). **(D–F)** Quantitative analysis of fractional anisotropy **(D)** and the underlying components of axial **(E)** and radial **(F)** diffusivity across preinjury and postinjury time points. Data represent values from the corpus callosum in coronal slices (0.5 mm × 2) corresponding to Slices 5 and 6 of the ex vivo analysis (see Fig. 2 for region-of-interest and coronal levels). FA and axial diffusivity values are significantly reduced after injury. *, $p < 0.05$ using one-way analysis of variance with post hoc comparisons to baseline. Values shown as mean ± SD. Scale bar = **(A–C**, shown in **C)** 1 mm.

Controlled cortical impact (CCI), which involves craniotomy and impact onto the dura over the cerebral cortex, is known to produce behavioral deficits on a beam walk task even with a mild severity of injury (36). Therefore, CCI was used as a positive control for behavioral assessment of impaired function of sensorimotor cortex when performed at the same coronal level of the bregma for comparison with the TAI model of skull impact at the bregma that is used throughout the current study. Controlled cortical impact was used to produce mild-moderate damage to the right sensorimotor cortex at the same coronal level of bregma. Mice (n = 21) were secured in the stereotaxic frame with ear bars and anesthetized as above. A 3-mm-diameter craniotomy was performed and a 2-mm-diameter impact tip was set at the following coordinates: 0 AP, 1.5 ML, −1.0 DV. Cortical impact was set at a velocity of 1.5 m/s and a dwell time of 100 ms.

Statistical Analysis

Immunohistochemistry quantification included at least 3 sections per mouse and at least 3 mice per condition. Imaging studies used cohorts of 5 mice per condition. Behavioral assessments involved between 6 and 27 mice per condition. Results of quantitative analyses were analyzed with Prism 5.0 (GraphPad Software). One-way analysis of variance with post hoc Tukey test was performed to determine significant differences across multiple time points. The longitudinal in vivo DTI study was analyzed by one-way analysis of variance with repeated measures. Significant differences between 2 groups for a given time point were determined using the Student t-test, with the exception of the AP intensity index, which was analyzed using the Mann-Whitney test for nonparametric data. χ^2 analysis was performed to verify significance between percentages. Statistical significance was determined as p < 0.05.

RESULTS

Surgical and Histopathologic Data

Three impact depths (1.0, 1.5, and 2.0 mm) were compared to determine the appropriate parameters for the analysis of TAI and CC integrity (Fig. 1). Increasing impact depth resulted in a longer duration of apnea and prolonged the time for the righting reflex (Fig. 1A, B). Skull fracture and bleeding severity increased, particularly with the depressed skull fractures observed at the 2.0-mm depth (Fig. 1C, D). These surgical and postsurgical indicators of injury severity corresponded well with histopathologic features (Fig. 1F–N). The 2.0-mm injury produced damage in the CC underlying the impact site (Fig. 1F) that extended caudally (Fig. 1I) and rostrally (Fig. 1L) with hemosiderin deposits indicating areas of prior hemorrhage (Fig. 1L). At the 1.5-mm depth, skull fractures were less severe than those at 2.0 mm and were typically linear or branched rather than depressed fractures (Fig. 1D). Mice with the 1.5-mm impact did not show impairment on the beam walk test in contrast to a positive behavioral control of mice subjected to a mild CCI injury, which involves a craniotomy and contusion damage of sensorimotor cortex (Fig. 1E). Following the 1.5-mm injury, cortical cavitation was absent (Fig. 1G, J) or minor and was associated with hemosiderin

aggregates indicating areas of prior bleeding (Fig. 1M, N). The CC exhibited potential areas of demyelination (Fig. 1J, K) without marked changes in cellularity (Fig. 1G). The 1.0-mm depth produced the least severe postinjury characteristics (Fig. 1A–D) but failed to produce consistent evidence of cortical or CC pathology (Fig. 1H and data not shown for Luxol fast blue and Prussian blue staining). Based on this characterization of injury severity, the 1.5-mm depth was determined to be the most relevant for further analysis of the CC, that is, to examine TAI without extensive concomitant pathology from cortical cavitation or focal white matter loss.

Ex Vivo DTI With Postimaging Immunohistochemistry Localizes CC Damage Over Ventricles

Ex vivo DTI was used to localize areas of tissue damage within the CC after the 1.5-mm impact. Postimaging immunohistochemistry was performed to distinguish specific pathologic features in the CC at coronal levels with significant DTI findings at 3 days after the 1.5-mm impact or sham surgery. Color-encoded FA maps illustrate the region of interest used for the analysis of the CC (Fig. 2A, B). The midline crossing of the anterior commissure is also visible and corresponds with the coronal level of the impact centered at bregma.

Coronal slices (0.5 mm thick) throughout the rostrocaudal extent of the CC were analyzed to quantify FA and the diffusion tensor derived components of axial ($\lambda_{\parallel}$ parallel to the fiber tract) and radial ($\lambda_{\perp}$; perpendicular to the fiber tract) diffusivity (Fig. 2C–E). A progressive variation of FA values was observed across coronal levels that may be associated with neuroanatomical changes in the CC thickness and fiber composition (26, 37). The FA values for injured mice were reduced but not significantly different from sham mice. Analysis of axial and radial diffusivity showed that a significant difference between injured and sham occurs only in axial diffusivity and was specifically found in coronal slices near the plane of the bregma, the point of impact.

In CC regions with reduced axial diffusivity, immunohistochemistry for βAPP showed a significant increase in the number of labeled axon profiles, indicating axonal damage (Fig. 2F). Microglial activation was also significantly increased based on CD11b immunoreactivity (Fig. 2G). Immunolabeling for GFAP was increased as well, indicating reactive gliosis (Fig. 2H). Widespread demyelination was not apparent based on the similarity of myelin immunoreactivity between the concussive brain injury and sham mice (Fig. 2I). The cell density was not altered between injured and sham mice (Fig. 2J).

In Vivo Longitudinal DTI Demonstrates Reduced CC Integrity Through the First Week After Injury

We next performed an in vivo longitudinal series of magnetic resonance scans to evaluate the progression of changes in the CC from preinjury baselines values across the first week after injury from the 1.5-mm impact (Fig. 3). The CC did not show overt structural changes with T2-weighted imaging. However, signal hyperintensity in T2-weighted imaging was
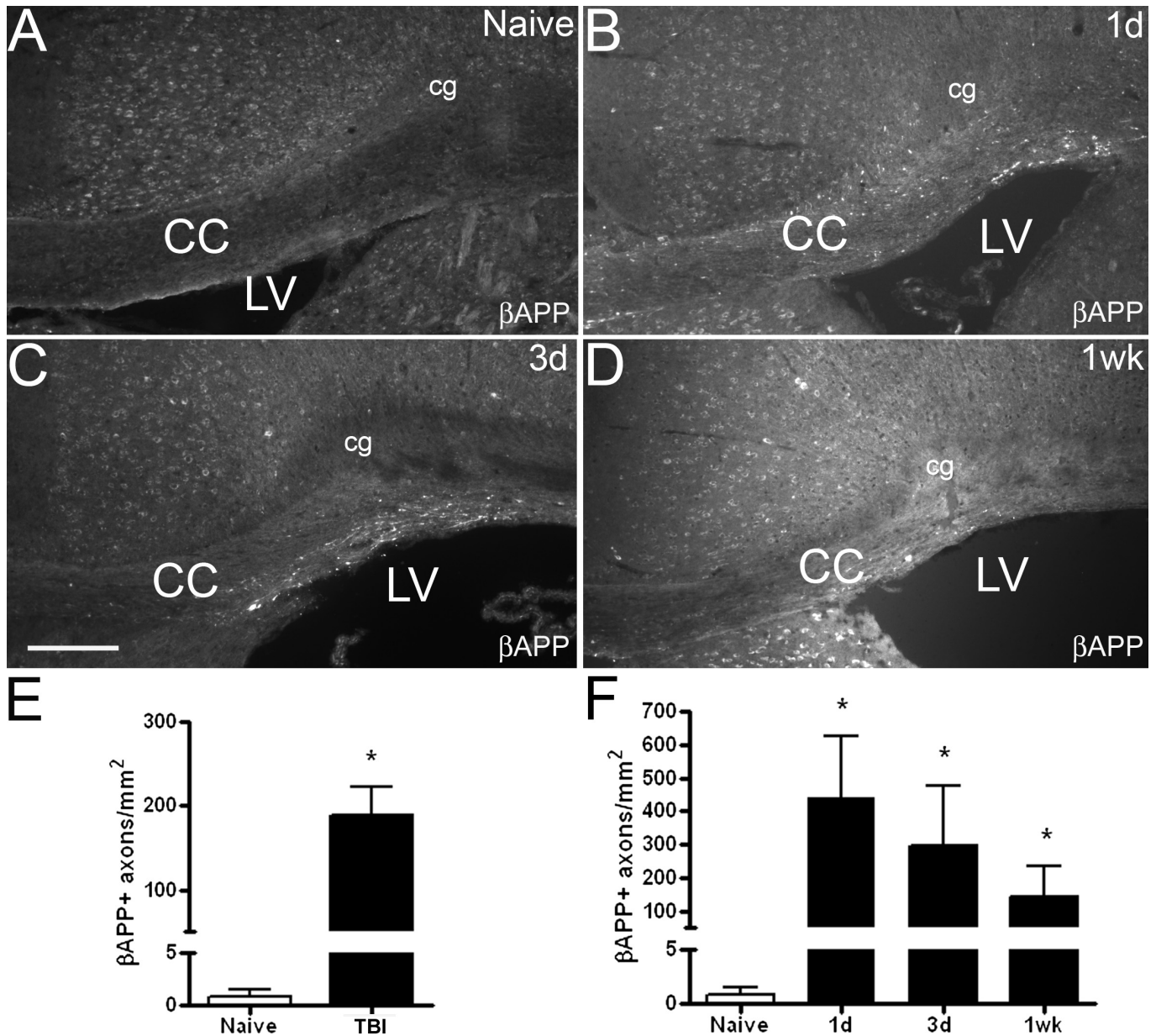
FIGURE 4. β-Amyloid precursor protein (βAPP) demonstration of impaired axonal transport in the corpus callosum (CC). **(A–D)** Immunohistochemistry on coronal brain sections for βAPP as an indicator of axon damage that is associated with impaired rapid axonal transport. In naive mice **(A)**, βAPP is present in the cytoplasm of cortical neurons but immunoreactivity in the CC reflects only background staining. Mice with 1.5-mm injury **(B–D)** show βAPP immunoreactivity in axonal swellings in the CC that are most prominent over the lateral ventricles (LV). **(E, F)** Quantification of the βAPP immunolabeled axons in the CC. Comparison of naive and concussive brain injury (CBI) mice at 1 week after injury **(E)** (*, $p < 0.05$; n = 5) from the cohort of mice used for the longitudinal diffusion tensor imaging (DTI) (Fig. 3). **(F)** In an analysis of βAPP within cohorts sampled at each of the time points used for MRI (naive/baseline, 1 day, 3 days, and 1 week after CBI; n = 3 mice per time point), a significant increase in βAPP indicates axon damage at each time point (*, $p < 0.05$ compared to naive). Scale bar = **(A–D**, shown in **C)** 200 μm. Cg = cingulum.

often observed in the superficial region of the cortex, particularly at coronal levels rostral to the impact (Fig. 3C; slice level is rostral to slices quantified for DTI and shows the same mouse with cortical hemosiderin deposits in Fig. 1N). In vivo DTI quantitative analysis of the CC focused on coronal levels corresponding to significant DTI differences identified in the ex vivo analysis (Fig. 2D; Slices 5 and 6).

Consistent with reduced white matter integrity, FA values in the CC were significantly reduced at 1, 3, and 7 days after TBI compared to baseline. Axial diffusivity values were also significantly decreased at each postinjury time point, whereas radial diffusivity was unchanged from baseline. Mice were perfused after the last in vivo MRI scans at 7 days after injury and examined by immunohistochemistry along with additional
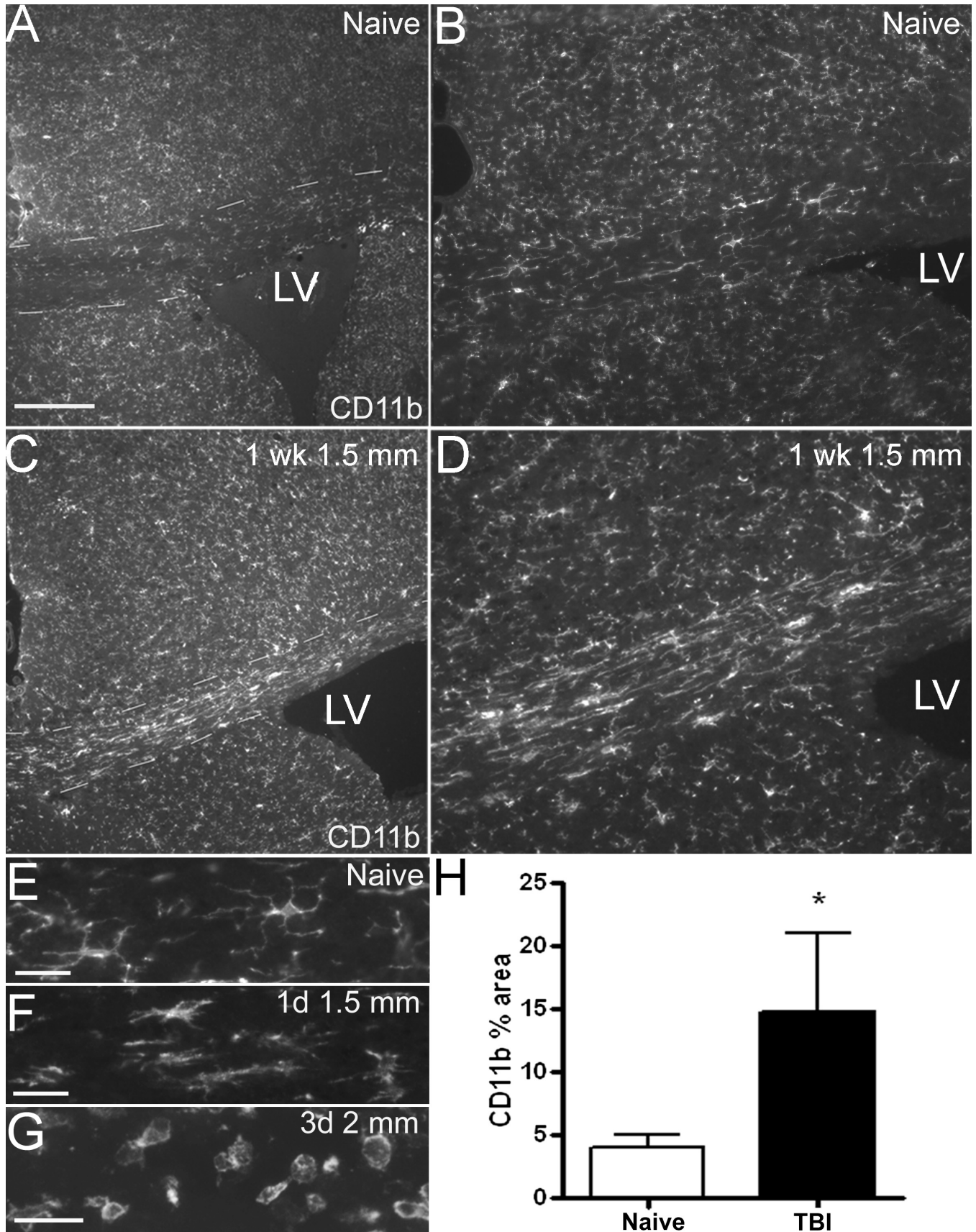
cohorts of mice to compare naive mice with the progression of changes at 1, 3, and 7 days after injury.

Acute TAI Is Present in the CC Through the First Week After Injury

βAPP accumulations in axons of the CC were significantly increased at all time points after the 1.5-mm impact (Fig. 4A–F). Therefore, the reduced FA and axial diffusivity values correspond with axon damage in the CC in the same mice analyzed after ex vivo (Fig. 2F; 3 days after injury) and in vivo imaging (Fig. 4E; 7 days after injury). An additional cohort of mice demonstrates βAPP accumulations in axons at each of the time points (1, 3, and 7 days after injury) corresponding to the longitudinal DTI study (Fig. 4F). βAPP accumulations were also observed in the cingulum and external capsule but not in the internal capsule (data not shown).

Microglia in CC Exhibit Hypertrophic Activation

The microglial response is an important element for interpreting the pathologic environment relative to the influence on DTI and the tissue milieu after TAI. CD11b immunohistochemistry was used to characterize microglia and macrophage activation after the 1.5-mm impact (Fig. 5). CD11b immunoreactivity was significantly increased in the CC in injured mice at 7 days after injury as compared to naive mice (Fig. 5). Interestingly, the morphology of the CD11b-immunolabeled cells in mice with the 1.5-mm impact indicated an intermediate hypertrophic stage of activation with thickened processes (Fig. 5D, F). This activation appeared within the first day and continued throughout the time points examined. With a 2.0-mm-depth impact, microglial activation progressed to a full ameboid stage (Fig. 5G). Therefore, microglial activation in the CC white matter corresponded more directly with injury severity than time after injury within this first week.

Proliferative Response in CC Is Distinct From Astrogliosis

Astrogliosis was characterized by expression of GFAP, cell morphology, and proliferation (Fig. 6). Glial fibrillary acidic protein expression was increased in the CC at 1, 3, and 7 days after injury (1.5 mm; Fig. 6A–D). Periventricular astrogliosis was present in injured mice but was not a consistent finding. Glial fibrillary acidic protein immunoreactivity showed marked staining of dense astrocyte processes in the CC in mice with TBI as compared to naive mice. Proliferation

is an indicator of progression to more severe stages of astrogliosis (38). Actively proliferating cells were identified by Ki67 immunolabeling (Fig. 6A-D). Cell proliferation was increased significantly in the CC at 1 and 3 days after injury (Fig. 6F). However, astrocyte proliferation (Ki67-positive/ GFAP-positive cells) was not significantly increased in injured mice at 1, 3, or 7 days versus naive mice (peak = 12.59 ± 3.91 [SD] cells/mm^2 at 1 day after injury).

NG2 Progenitor Proliferation Increases in the SVZ and CC After TBI

The SVZ is a source of neural stem cells that can replace cells in the adjacent CC after damage. Ki67 immunohistochemistry showed similar levels of cells actively dividing in the SVZ throughout the first week after injury (Fig. 7A). To examine the SVZ neural stem cell response between preinjury and postinjury stages, BrdU was administered 1 day before injury and then mice were perfused at 1, 3, or 7 days after injury. BrdU labeling in the SVZ was similar at each time point between paired injured and naive cohorts (Fig. 7B–D). Therefore, the severity of this TBI was not sufficient to stimulate an overall proliferative response in the SVZ.

Among the neural cell types generated from the SVZs, the OP population is specifically relevant to CC white matter damage. Therefore, BrdU incorporation was examined among OP cells identified by NG2 immunolabeling (Figs. 7E–H and 8). In the SVZ region, OP proliferation was initially reduced but increased significantly by 3 days after injury (Fig. 7H), indicating potential induction of oligodendrocyte lineage cell generation from neural stem cells of the SVZ. Within the CC, proliferation of OP cells was increased 3 and 7 days after injury (Fig. 8F, G). Furthermore, by 1 week after injury, the OP population was significantly increased in the CC in comparison with the matched naive cohort (Fig. 8H).

Oligodendrocytes Shift Transcriptional Activation After TBI

In situ hybridization for PLP mRNA was used to examine the oligodendrocyte response to the 1.5-mm impact (Fig. 9). During myelination and remyelination, oligodendrocytes upregulate transcription of myelin genes, with PLP being the most abundant myelin gene. Therefore, the presence of PLP mRNA signal was used to identify oligodendrocytes, whereas the signal intensity and distribution provided additional indications of transcriptional activity. Oligodendrocytes were classified according to PLP transcript expression being

FIGURE 5. Microglia/macrophage activation within the corpus callosum. **(A–D)** Immunohistochemistry for CD11b to detect microglia/macrophage cells in coronal sections from noninjured naive mice **(A, B)** and mice at 1 week after 1.5-mm skull impact **(C, D)**. The corpus callosum is indicated by hashed lines in **A** and **C**. **(E–G)** Higher-power images illustrate the range of reactive morphologic changes of CD11b-immunolabeled cells in the corpus callosum. CD11b cells in naive mice have fine elaborate processes **(E)**. CD11b-immunolabeled cells have more condensed processes after 1.5-mm skull impact that is present from 1 day **(F)** through 1 week **(D)** after injury. After a 2.0-mm impact, more severe reactive changes are associated with a rounded morphology and lack of processes among CD11b-immunolabeled cells **(G)**. **(H)** Quantification of CD11b immunoreactivity in the corpus callosum shows a significant increase in microglia/macrophage activation at 1 week after TBI (1.5-mm impact) compared to naive control mice (*, p = 0.0122; n = 5). Quantification shows postimaging tissue analysis from the cohort of mice used for the longitudinal diffusion tensor imaging (DTI) (Fig. 3). Scale bars = **(A, C**, shown in **A)** 200 μm; **(B, D**, shown in **B)** 75 μm; **(E–G)** 40 μm. LV = lateral ventricle.
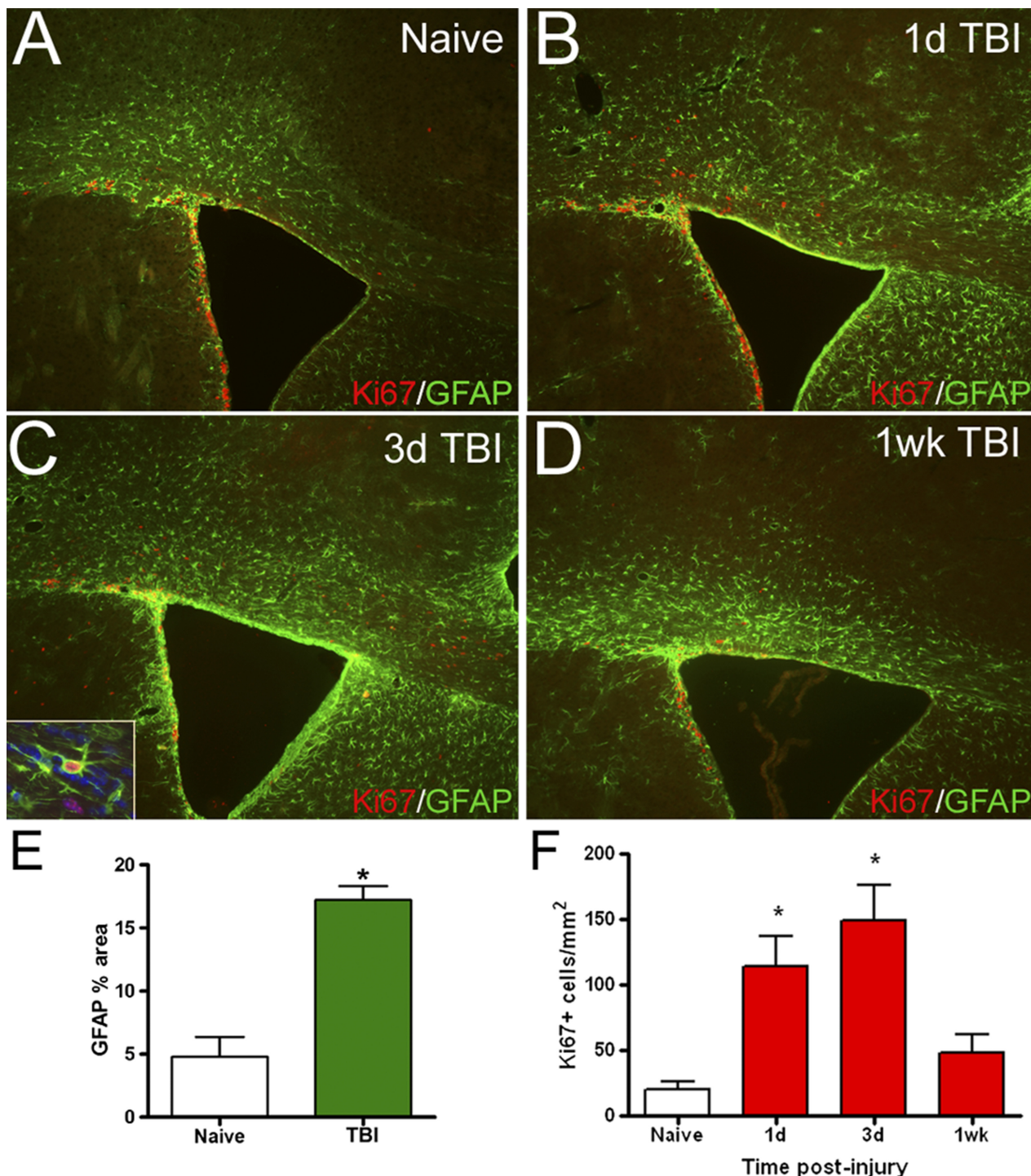
FIGURE 6. Astrogliosis and cell proliferation within the corpus callosum after traumatic brain injury (TBI). **(A–D)** Immunohisto-chemistry in coronal brain sections to detect actively dividing cells with Ki67 and evaluate astrogliosis based on the expression of glial fibrillary acidic protein (GFAP). Ki67 shows proliferating cells within the subventricular zone at all time points **(A–D)** and in the corpus callosum mainly at 1 and 3 days after TBI **(B, C)**. GFAP expression is increased through 1 week after TBI **(B–D)** versus naive conditions **(A)**. Proliferating cells include reactive astrocytes **(C**, inset**)**, but relatively few cells are double labeled (GFAP-positive, Ki67-positive). **(E)** Quantification of GFAP immunolabeling indicates that reactive gliosis is significantly increased in the corpus callosum 1 week after injury (*, $p < 0.0001$; n = 5). This quantification shows values obtained after imaging for the cohort of mice used in the longitudinal diffusion tensor imaging (DTI) study (Fig. 4). **(F)** Quantification of Ki67-immunolabeled cells within the corpus callosum shows proliferation is significantly increased at 1 and 3 days after injury and returns to baseline values at 1 week (*, $p < 0.05$ compared to naive; n = 3 per time point). Scale bar = **(A-D**, shown in **D)** 200 μm. LV = lateral ventricle.
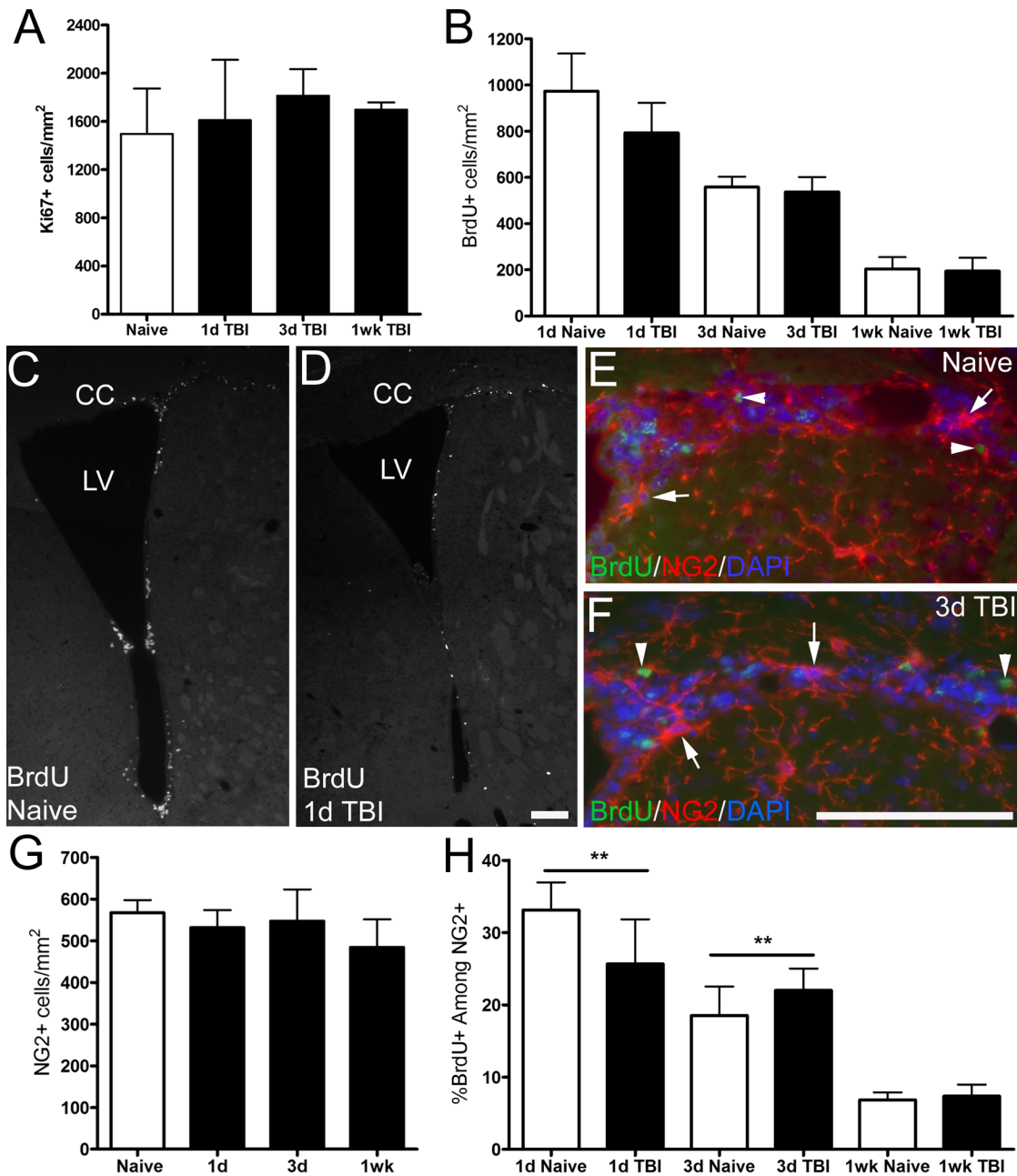
FIGURE 7. Proliferation within the subventricular zone after traumatic brain injury (TBI). **(A–D)** Overall proliferation within the subventricular zone (SVZ) was quantified using Ki67 to immunolabel actively dividing cells **(A**, images in Fig. 6**)** and a BrdU pulse-chase protocol to label endogenous cycling cells before injury and monitor the postinjury response **(B–D)**. The density of Ki67-immunolabeled cells in the SVZ is similar across post-TBI (1.5-mm impact) time points, indicating that there is not a significant difference of cells actively dividing within the SVZ at the time of tissue analysis (p = 0.702; n = 3 mice per time point) **(A)**. BrdU was administered 1 day before TBI, and cells were analyzed in the SVZ at 1, 3, and 7 days after TBI **(B–D)**. Age-matched naive mice were injected with BrdU and perfused in parallel. Quantification of BrdU immunohistochemistry shows similar values in the SVZ for each time point **(B**, for each time point, n = 3 naive, n = 5 injured**)**. Coronal sections illustrating BrdU-immunolabeled cells in the SVZ for a BrdU pulse-chase shown at 1 day after TBI **(D)** and for a matched naive mouse **(C)**. **(E–H)** NG2 immunohistochemistry to determine the oligodendrocyte progenitor response in the SVZ relative to axonal injury in the overlying corpus callosum (CC). Coronal sections illustrate BrdU pulse-chase shown at 3 days after TBI **(F)** and at matched time point for a naive mouse **(E)**. Arrows denote examples of NG2 cells in SVZ. Arrowheads indicate examples of BrdU-labeled nuclei **(E, F)**. The total NG2 cell density remained constant throughout the first week after injury **(G)**. The proportion of NG2 cells labeled with BrdU indicates that the proliferative response changes significantly in the injured mice relative to the matched naive time points **(H; **,** p = 0.0047 for 1 day; p = 0.0058 for 3 days; n = 3 naive and n = 5 TBI for each time point). Scale bars = **(C, D**, shown in **D)** 100 μm; **(E, F**, shown in **F)** 100 μm. LV = lateral ventricle.
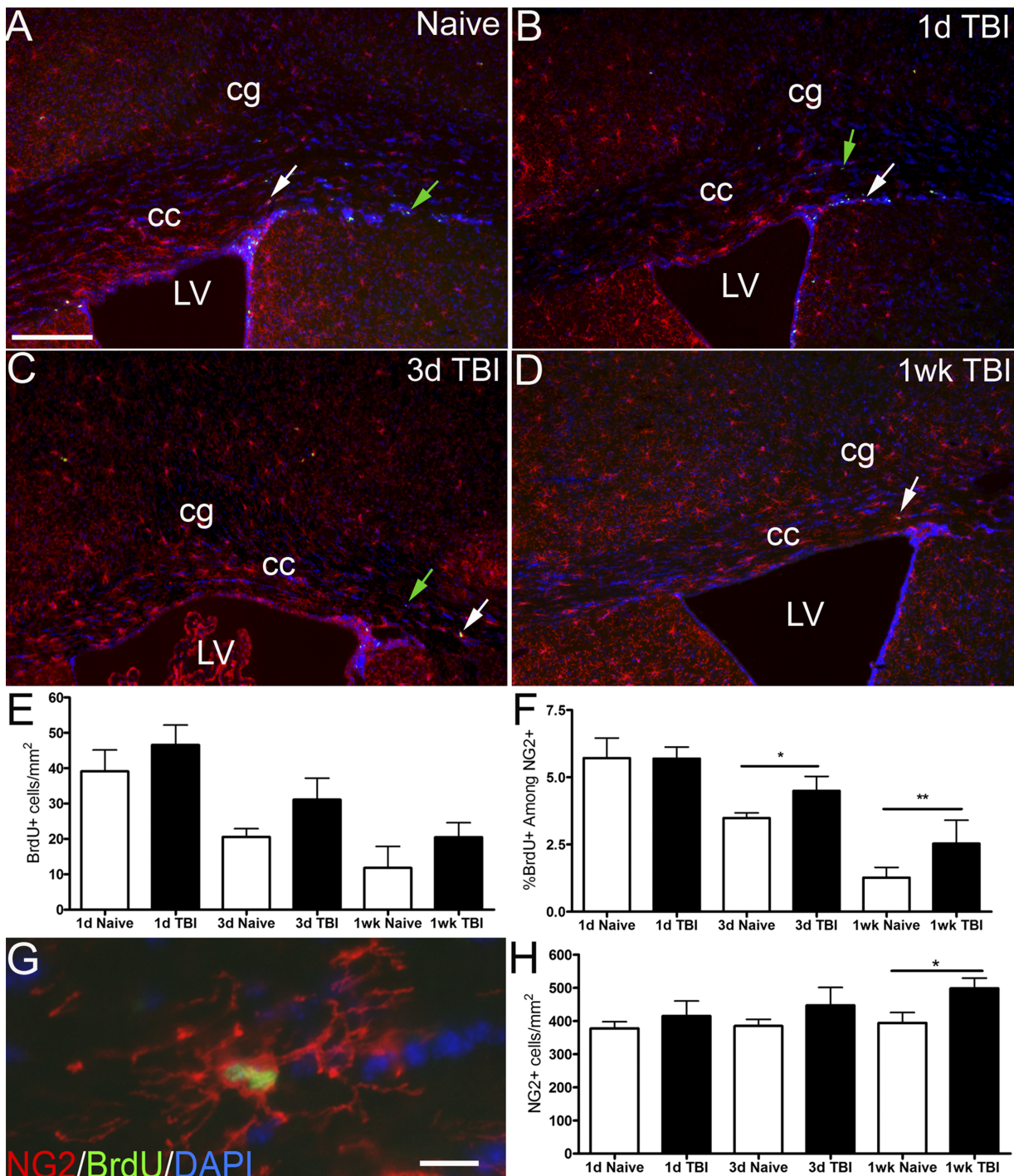
FIGURE 8. Oligodendrocyte progenitor population increases within the corpus callosum after traumatic brain injury (TBI). (A–D) Immunohistochemistry for oligodendrocyte progenitors, identified by NG2 (red) and BrdU (green) to detect proliferation in coronal brain sections. BrdU was administered on the day before TBI (1.5-mm impact). Mice were perfused on Days 1 (B), 3 (C), and 7 (D) after injury. Age-matched naive mice (A) were injected with BrdU and perfused in parallel. Green arrows show examples of cells immunolabeled only for BrdU. White arrows show examples of cells double labeled for BrdU and NG2. (E) BrdU immunolabeling in the corpus callosum appears higher after injury but does not reach significance (p = 0.0709). (F) The proportion of NG2 cells that have detectable BrdU increases at 3 and 7 days after TBI (*, p < 0.05; **, p < 0.01, respectively). (G) Double labeling for BrdU (green) in the nucleus and NG2 (red) on the cell body and processes along with DAPI nuclear staining (blue). Example shown is the cell at the arrow in D. (H) The total NG2 population is significantly increased at 7 days after TBI versus naive values (*, p < 0.05). For each value shown (E, F, H), n = 3 naive mice and n = 5 mice with TBI at each time point. Scale bars = (A–D, shown in A) 200 μm; (G) 15 μm. CC = corpus callosum, cg = cingulum, LV = lateral ventricles.
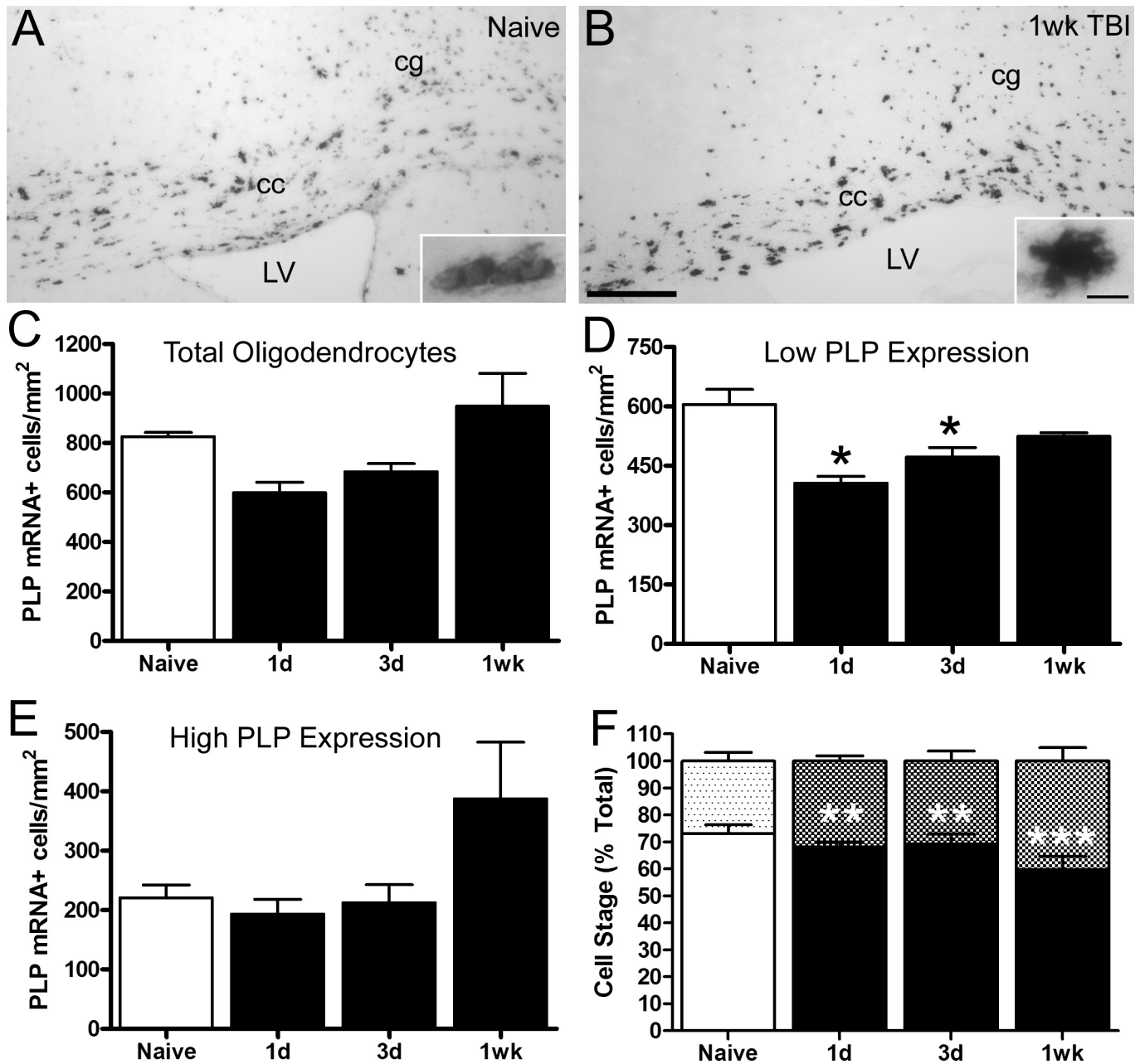
FIGURE 9. Myelin proteolipid protein (PLP) transcription is altered in oligodendrocytes of the corpus callosum after traumatic brain injury (TBI). In situ hybridization for PLP mRNA in coronal sections from mice perfused at 1 day, 3 days, and 1 week after TBI (1.5-mm impact) were compared to naive mice. **(A, B)** Coronal sections illustrating PLP transcripts in naive **(A)** and 1 week post-TBI mice **(B)**. Insets show examples of oligodendrocytes with low **(A**, inset**)** and high **(B**, inset**)** levels of PLP mRNA signal. **(C–E)** Quantification in the corpus callosum for the total number of PLP-expressing oligodendrocytes **(C)**. Oligodendrocytes with a low level of PLP transcripts are more abundant in normal adult mice **(D)** than oligodendrocytes with high PLP expression **(E)**. Sample size of cohorts was n = 3 (naive and 1 day after TBI), n = 4 (3 days after TBI), and n = 5 (1 week after TBI). The density of total oligodendrocytes does not differ significantly across time points **(C**; p = 0.0949**)**. The number of oligodendrocytes with low levels of PLP transcript decreased 1 and 3 days after injury **(D**; *, p < 0.05**)**. Oligodendrocytes that expressed high levels of PLP mRNA were increased at 1 week after TBI but not significantly different **(E**; p = 0.1769**)**. **(F)** Analysis of the proportion of PLP low- and high-expressing cells shows a significant shift that takes into account the simultaneous changes in both populations at a given time point **(F**; **, p < 0.001; ***, p < 0.0001**)**. Scale bars = **(A, B**, shown in **B)** 200 μm; (inserts in **A** and **B**, shown in insert **B)** 10 μm. CC = corpus callosum, cg = cingulum, LV = lateral ventricle.
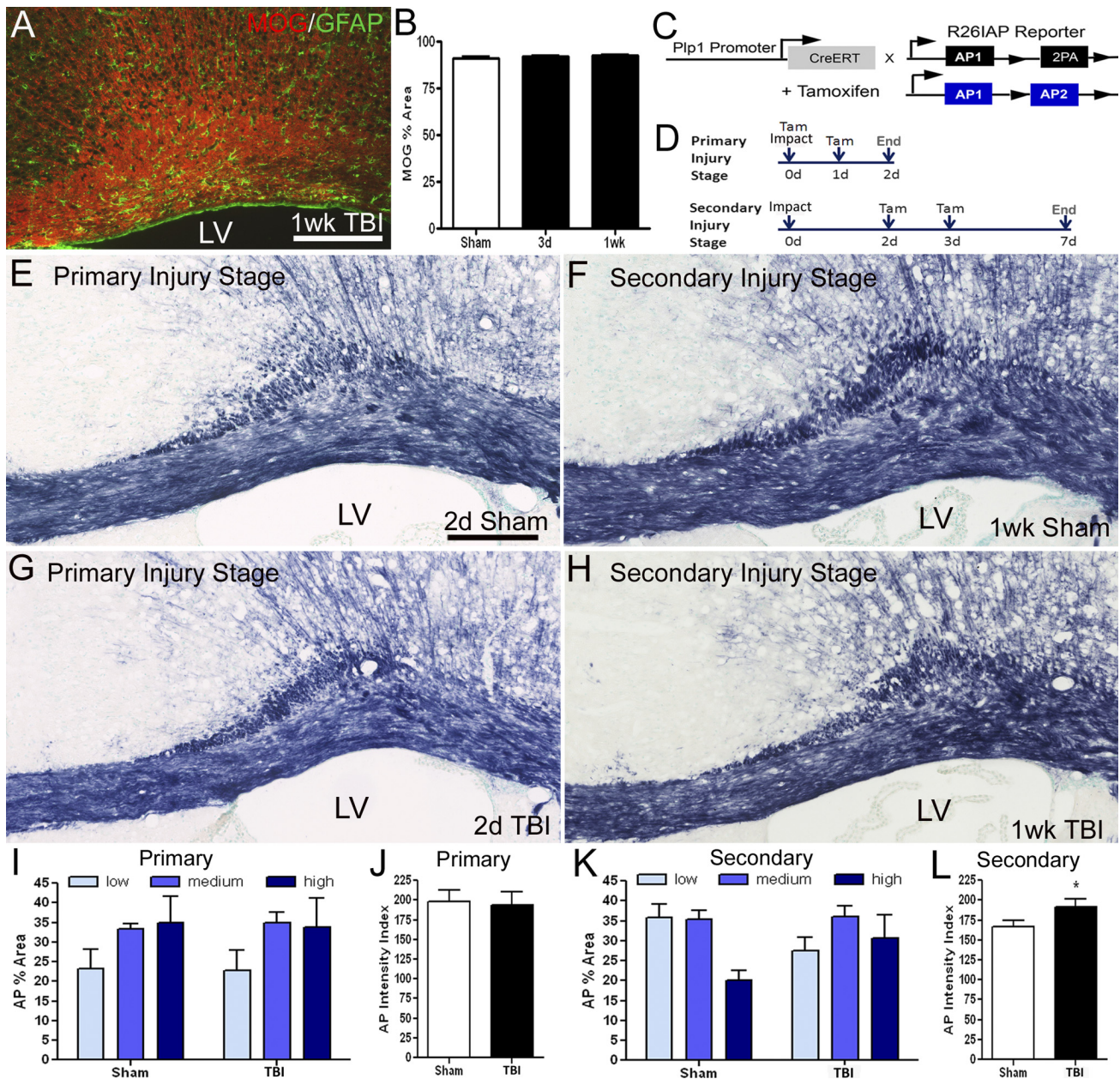
FIGURE 10. The oligodendrocyte-myelin unit is altered during the secondary injury stage after traumatic brain injury (TBI). **(A, B)** A coronal section immunolabeled for myelin oligodendrocyte glycoprotein (MOG) to detect myelin and for glial fibrillary acidic protein (GFAP) to examine astrogliosis. MOG immunoreactivity appeared less intense in regions of astrogliosis **(A)**, but the myelinated area in the corpus callosum was not significantly different between sham and mice with TBI throughout the first week of injury **(B)**. **(C–L)** *Plp/CreER^T:R26IAP* reporter mice were used to test the ability of oligodendrocytes to synthesize alkaline phosphatase (AP; a membrane-associated reporter molecule), transport AP along processes, and incorporate AP into myelin sheaths **(C)**. *Plp/CreER^T:R26IAP* mice were administered tamoxifen to induce recombination and expression of AP via inversion of the floxed AP second exon. Tamoxifen (Tam) induction was used to visualize AP labeling of myelin during either a primary injury stage (0–2 days) or during a secondary injury stage (2–7 days) **(D)**. AP incorporation into myelin was apparent as a blue substrate reaction in coronal brain sections, particularly in the corpus callosum **(E–H)**. **(I–L)** Quantification of the area of AP labeling took into account variation in the intensity of signal among regions of the corpus callosum. During the primary injury stage, the sham and TBI (1.5 mm impact) mice had similar proportions of labeling within the corpus callosum for all AP intensities **(I)**. During the secondary injury stage, the overall proportion of the corpus callosum labeled was not different, but there was a shift among the areas based on AP intensity **(K)**. A weighted AP intensity index **(J, L)** was used to semiquantitatively compare the AP-labeled areas while taking into account the relative area exhibiting low, medium, and high AP levels. The AP intensity index is significantly increased in TBI versus sham only mice during the secondary injury phase **(L; *, p = 0.0260)**. Sample size of cohorts was n = 12 for was primary injury stage (6 sham, 6 TBI) and n = 11 for secondary injury stage (5 sham, 6 TBI). Scale bars = **(A)** 200 μm; **(E–H**, shown in **E)** 200 μm.

low (Fig. 9A, inset) or high (Fig. 9B, inset). The total oligo-dendrocyte population decreased by approximately 30% within 1 day after injury (Fig. 9C). Low PLP mRNA-positive cells represent the majority (73.14% ± 5.4%) of the oligo-dendrocyte population in the normal CC of naive mice and were significantly decreased at 1 and 3 days in injured mice (Fig. 9D). At 7 days after injury, high PLP-expressing cells were visually notable (Fig. 9B). A shift toward an increase in high versus low PLP expression in injured vs. naive mice was significant at all postinjury time points and most prominent at 1 week (Fig. 9D–F).

Integrity of Myelin-Oligodendrocyte Unit After TBI

Immunohistochemistry for MOG myelin protein corre-lates well with electron microscopy and Luxol fast blue myelin stain for quantification of focal demyelination within the mouse CC (28, 39). However, after the 1.5-mm impact injury, MOG immunohistochemistry did not detect differences in the extent of myelination within the CC (Fig. 10A, B). Reduced intensity of MOG immunoreactivity was often noted, but focal regions of frank myelin loss were not evident. During this first week after injury, MOG immunoreactivity could reflect intact mye-lin, but degenerating myelin could also stain along axons be-fore phagocytosis and clearance (40).

To evaluate the integrity of the myelin-oligodendrocyte unit after injury more specifically, we developed a novel ap-proach using *Plp/CreER^T* driver mice crossed to *R26IAP* reporter mice. The *Plp/CreER^T:R26IAP* mice conditionally express the AP membrane protein after tamoxifen adminis-tration (Fig. 10C). After the 1.5-mm impact injury, *Plp/CreER^T:R26IAP* mice were examined with tamoxifen treat-ment protocols designed to evaluate oligodendrocyte syn-thesis and translocation of AP into myelin during either a
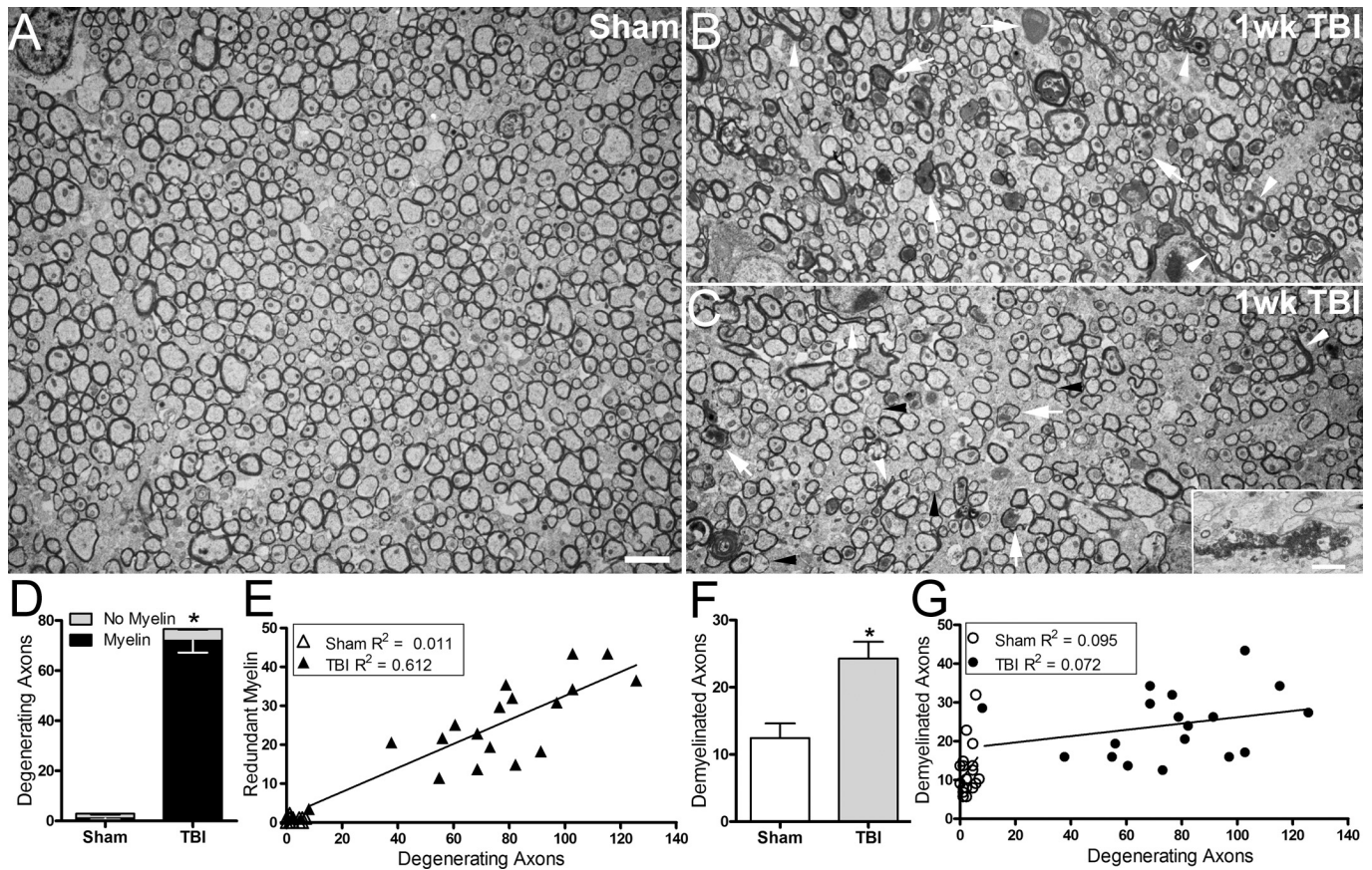

FIGURE 11. Electron microscopy of the corpus callosum illustrates axon and myelin changes after traumatic brain injury (TBI). **(A–C)** Sagittal sections of the corpus callosum from sham **(A)** and 1 week after TBI **(B, C**; 1.5-mm impact**)**. A normal distribution of myelinated fibers is shown in the sham mouse **(A)**. After TBI, axon degeneration (white arrows; **B, C**) is prominent. Degenerating axons exhibit swellings with accumulation of vesicles (inset; **C**). Examples of demyelinated fibers are also apparent in images from the mice with TBI (black arrowheads; **B, C**). The TBI tissues also had notably elongated, redundant myelin figures (white arrow-heads) associated with degenerating axons (**B**, arrowhead furthest to right) or void of an axon (**B**, arrowhead along bottom). **(D–G)** Quantification of axon and myelin pathology. Axon degeneration was significantly increased at 1 week after injury (1.5 mm) versus sham (p < 0.0001 for total fibers), which was mainly associated with myelinated fibers (p < 0.0001 fibers with myelin, black; p < 0.0058 fibers without myelin, gray) **(D)**. Redundant myelin figures were highly correlated with degenerating axons in mice with TBI **(E)**. Demyelinated axons were significantly increased in mice with TBI **(F)**, but this did not correlate with the frequency of degenerating axons **(G)**. Sample size of cohorts was n = 3 for each condition, sham, and TBI at 1 week after surgery. Scale bars = **(A–C**, shown in **C)** 2 μm; **(**inset in **C)** 2 μm. Values shown are squared millimeter × 10^3.

© 2013 American Association of Neuropathologists, Inc.

primary injury stage (0–2 days) or a secondary injury stage (2–7 days) (Fig. 10D). This approach demonstrated that AP labeling of myelin in the CC during the primary injury stage was similar between injured and control mice (Fig. 10E, G, I, J). Therefore, oligodendrocyte processes to myelin sheaths are not significantly disrupted by the initial impact injury. During the secondary injury phase, AP-labeled regions had proportionally higher signal intensity values in the injured mice, which resulted in a significant increase in the AP intensity index compared to sham mice (Fig. 10F, H, K, L).

Ultrastructural Evidence of Myelin Abnormalities and Axon Damage After Injury

Electron microscopy of the CC was used to investigate changes related to myelination and the correlation with TAI after the 1.5-mm impact injury (Fig. 11). Sagittal sections from sham mice illustrate the small diameter and thin myelin of axons in the CC over the lateral ventricles (Fig. 11A). Corpus callosum regions from mice 1 week after injury exhibited degenerating axons with dark axoplasm and accumulation of vesicles, indicative of disrupted axonal transport (Fig. 11B, C). The majority of degenerating axons still had visible myelin, which often was split or ballooned off the remaining axon segment (Fig. 11C). Myelin sheaths were often collapsed around a dystrophic axon or back onto themselves if the axon was no longer present. Extensive myelin figures that resembled redundant myelin sheaths were significantly increased in the injured tissue (sham = $0.63 \pm 0.1269/mm^2 \times 10^3$, TBI = $25.37 \pm 4.055/mm^2 \times 10^3$; p = 0.0037; Fig. 11D). These redundant myelin figures were distinctive for the large extent of myelin, usually folded back onto itself, well beyond simple sheath collapse (Fig. 11B, C). Redundant myelin figures were highly correlated with degenerating axons (Fig. 11E). Demyelinated axons were also more prevalent in the injured tissues (Fig. 11F) (sham = $12.43 \pm 2.16/mm^2 \times 10^3$, TBI = $24.29 \pm 2.47/mm^2 \times 10^3$; p = 0.0226). However, demyelination did not correlate specifically with the frequency of degenerating axons (Fig. 11G).

DISCUSSION

The current study interrogates white matter integrity using DTI and multiple methods of tissue analysis to characterize the complement of dynamic cellular responses to TAI in the CC. This is the first demonstration of oligodendrocyte lineage changes from neural stem cell through myelination in the context of white matter TAI without extensive concomitant pathology from cortical cavitation or focal white matter loss.

Surgical and neuroimaging data establish important benchmarks for reproducibly generating CC TAI pathology and for comparison with other studies of experimental TBI (Figs. 1–3). The electrically controlled impact device provides a relatively consistent system, but variation in using impactor devices cannot be avoided, even with the same manufacturer and model device. High-speed video recording of the impact was used to improve calibration across cohorts in the current study (data not shown). Variation could be reduced by excluding mice based on specific parameters, such as depressed skull fractures, which correspond with more severe bleeding. However, linear skull fractures may be considered an interesting component of the impact injury because skull fractures are found in more than 30% of mild-moderate human TBI cases (41).

Magnetic resonance imaging provided important cross-sectional and longitudinal data throughout the first week after TBI (Figs. 2 and 3). T2-weighted imaging indicated normal CC structure but showed initial signal hyperintensity in the rostral cerebral cortex that largely resolved between 3 and 7 days after the 1.5-mm impact (Fig. 3C–F). This suggests possible edema in the superficial cortex immediately below the impact site. In a similar injury model involving the posterior CC, measurement of tissue water content demonstrated cortical edema that did not extend to involve the hippocampus or thalamus (21). Our studies also show that cell density in the CC is not changed at 3 days after injury (Fig. 2J). These findings support a lack of detectable CC edema in this TAI model. The CC also did not exhibit marked hemorrhages, which could be detected in the superficial cortex by variable extents of hemosiderin in macrophages (Fig. 1M–N). Our DTI studies show that axial diffusivity was reduced throughout the first week after TBI while radial diffusivity was unchanged. These DTI measures may be less predictive of axon and myelin changes in conditions of edema, hemorrhage, and/or increased cell density from inflammation (23). However, these conditions in the CC do not seem to be significant with this injury at the time points examined. Our DTI data and tissue analysis of cellular responses to TAI should be useful for analyzing the progression of TBI pathology over time and for comparing the advantages of other neuroimaging techniques in detecting more complex pathologies. Our findings of reduced axial diffusivity (Figs. 2 and 3) are consistent with findings in the CC after repetitive, mild, closed head trauma producing mild axonal damage with microglial activation (42). Radial diffusivity is often increased in demyelinating conditions (26, 43), and the lack of change in the current study is important for correlation with the dispersed pattern of limited demyelination observed (Figs. 10 and 11).

The axon damage in the CC at this early injury stage shows impaired fast axonal transport occurring in a diffuse pattern. Immunoreactivity for βAPP, which accumulated in axons after injury (Fig. 4), detects βAPP in vesicles carried by fast axonal transport (44). Accumulation of βAPP in axons within 1 day after TBI (Fig. 4F) is consistent with the timing of βAPP accumulation in the CC in a rat model of impact acceleration TBI (31). Electron microscopy also provided ultrastructural evidence of vesicle accumulation in degenerating axons at 1 week after injury (Fig. 11B, C). This analysis demonstrated a pattern of degenerating axons interspersed among populations of apparently intact axons, as is typical of TAI associated with diffuse axonal injury in human white matter after TBI (1, 6). Additional approaches would be required to detect the full extent of axon degeneration in the CC (45–47). By clearly demonstrating impaired axonal transport by βAPP and electron microscopy, the current findings can be interpreted as reproducibly producing limited TAI in the CC to examine the subsequent cellular and neuroimaging changes of white matter. However, the current studies do not attempt to examine very early time points or events initiating

TAI because mechanical forces that initiate TAI in gyrencephalic human brain may not be appropriately replicated in lissencephalic mice (6, 48).

Astrogliosis and microglial activation were observed during the first week after TAI. Astrocyte reactivity included hypertrophy and disruption of distinct territories without a significant increase in proliferation (Fig. 6). Microglia became hypertrophic but did not progress to ameboid morphology (Fig. 5). In a subset of mice subjected to a deeper 2-mm impact injury, ameboid microglia were prevalent in regions of hemorrhage indicated by hemosiderin aggregates (Figs. 1L and 5G). Similar to our results, human TBI specimens also do not typically exhibit ameboid microglia in the CC during the acute stage (19). Microglial activation may increase when TBI is experienced at an older age (49) or after a second concussive injury (50). In addition, microglia may become activated early after a single injury and, subsequently, transition to an ameboid state with persistent activation during subacute through chronic stages in cases of diffuse TAI (19, 51). The majority of cell death observed in chronic TBI white matter is composed of activated microglia, which may also have a ''by-stander'' effect in causing continued oligodendrocyte cell death (52). Myelin debris also stimulates microglial neuroinflammation (18). These complex cellular interactions of microglia, oligodendrocytes, and myelin may initiate during the acute stage and contribute to a cycle of perpetuating white matter pathology.

Limited demyelination was present in this early-stage CC injury, consistent with a lack of ameboid microglial morphology that would correspond with significant phagocytosis of myelin debris. Demyelinated fibers were identified by electron microscopy as distributed among adjacent intact myelinated fibers (Fig. 11C). Corpus callosum areas under the cingulum often showed reduced myelin staining with Luxol fast blue (Fig. 1K). Focal regions of frank demyelination were not observed with the 1.5-mm impact depth (Figs. 1J and 10) but were produced with a more severe injury from the 2.0-mm depth (Fig. 1F, I). These findings indicate that focal myelin loss is mainly associated with more severe TAI and white matter hemorrhage or neuron cell body damage (1, 53). However, even with moderate forms of TAI, oligodendrocyte loss has been demonstrated and may be due to caspase 3-mediated cell death mechanisms (11).

Our data demonstrate that TAI in the CC resulted in an early loss of oligodendrocytes (Fig. 9D) followed by OP proliferation (Figs. 7H and 8F) and a phenotypic shift of oligodendrocytes toward increased transcription of myelin genes (Fig. 9F). These changes indicate a potential regenerative response after white matter injury. Studies in MS models of experimental demyelination of the CC have shown that OP cells are generated from neural stem cells of the SVZ and/or from proliferation of resident cycling cells within the CC. Importantly, these OP cells are capable of differentiating into oligodendrocytes during remyelination (14, 54, 55). Overall, cell proliferation in the SVZ was not stimulated by TAI, based on Ki67 immunolabeling up to 1 week after injury (Fig. 7A). This finding is consistent with rat fluid percussion data for Ki67 in the SVZ that showed no difference at 2 weeks followed by an increase at 6 months (56). Within the overall SVZ response, we identified changes relevant to white matter injury using NG2 to identify early OP cells and administering BrdU before injury for incorporation into endogenous cycling cells to avoid reactive proliferation of astrocytes and microglia. This approach detected increased proliferation of OP cells in the SVZ at 3 days after injury followed by an increase in the CC at 3 and 7 days and an increase in total NG2 cells that occurred in the CC by 7 days. Controlled cortical impact injury also resulted in a significant increase in NG2 cells in the CC but with an opposite time course that was significantly increased at 1 day after injury and resolved by 7 days (57). This difference may reflect a rapid reactive OP response after damage to cortical neuron cell bodies with CCI as compared to our data of TAI injury within the white matter that stimulated a proliferative response to generate an increase in the number of OP cells by 7 days. A study using tcf4 to identify OP cells using a moderate-severe fluid percussion model of TBI also reported increases in the CC (53); however, these tcf4 cells are difficult to interpret as OP cells since colabeling was not found with Olig2, which labels cells at all stages of the oligodendrocyte lineage. Prior studies of oligodendrocyte and OP responses in the CC have not been combined with the approaches used here to interpret potential regenerative changes of proliferation, myelin gene upregulation, or SVZ changes.

A shift toward a higher level of PLP transcription and AP labeling in *Plp/CreER^T:R26IAP* mice suggests activation of oligodendrocyte synthesis after TAI. Oligodendrocyte processes appear intact after the impact injury since AP labeling of myelin was not reduced during the 0- to 2-day period (Fig. 10J). This novel approach definitively distinguishes active oligodendrocyte protein synthesis and transport to myelin that could not be otherwise detected as occurring specifically during this 0- to 2-day period. During the subsequent 2- to 7-day postinjury period, AP labeling shifted from low to high levels (Fig. 10L). Importantly, our findings of oligodendrocytes with high levels of PLP mRNA transcripts are similar to the observations of remyelination in experimental models of MS (27, 28). An increased density of oligodendrocytes with high PLP mRNA levels (Fig. 9F) indicates increased PLP promoter activity to drive Cre recombinase expression, which remains active after tamoxifen administration, and therefore increases the probability of AP expression between 2 and 7 days after injury. Differences in the AP labeling of myelin sheaths could also indicate differences in the proportion of noncompact versus compact myelin after TBI. Noncompact myelin can have components move by lateral diffusion in the membrane as well as vesicular transport in the cytoplasm, whereas compact myelin is a barrier to vesicular transport (58). Therefore, higher AP levels may be observed when new oligodendrocyte processes are being elaborated, whereas low AP levels may correspond with areas of compact mature myelin.

Ultrastructural demonstration of remyelination by electron microscopy would require a longer postinjury period for remyelination to progress and would also be extremely challenging to quantify in view of the distributed pattern of axon damage and demyelination in this model along with the very thin myelin and small axon diameters of the mouse CC (13). Interestingly, we observed extensive myelin associated with

degenerating axons or absent of an intact axon (Fig. 11B). These structures resemble redundant myelin sheaths that have been attributed to excess myelin outgrowth during myelin formation or in conjunction with changes in axon diameter (59, 60). Analyses of demyelination and remyelination should take into consideration the volume of excess myelin membrane in these abnormal myelin sheaths, which could skew quantitative measures such as western blot analyses.

The first week after injury examined in the current study sets the stage for the progression to recovery versus chronic disease. The diverse glial cell responses to TAI indicate different potential contributions to pathologic outcome. The astrogliosis and microglial activation are relatively mild during this first week, which could present an opportunity to prevent transition to a more aggressive neuroinflammatory environment. Oligodendrocyte progenitor proliferation and oligodendrocyte upregulation of myelin synthesis are required for remyelination that can protect viable axons and restore function. However, myelin synthesis may also be a maladaptive response if myelin forms in excess in association with degenerating axons. Extensive abnormal myelin figures were observed in the current pathology so that subsequent degradation and production of myelin debris is a concern for exacerbating the microglial response. Productive remyelination requires postinjury periods of 2 or more weeks to evaluate effectively and may require specialized approaches, such as remyelination reporter mouse lines to distinguish newly formed myelin as demonstrated after spinal cord injury (13). Further studies of these cellular responses to TAI in later stages after TBI will be important to determine factors that exacerbate or attenuate progression to chronic neurodegenerative processes and to further develop neuroimaging for differentiating the complexity of ongoing neuropathology in TBI.

REFERENCES

1. Roozenbeek B, Maas AI, Menon DK. Changing patterns in the epidemiology of traumatic brain injury. Nat Rev Neurol 2013;9:231–6
2. Adams JH, Doyle D, Ford I, et al. Diffuse axonal injury in head injury: Definition, diagnosis and grading. Histopathology 1989;15:49–59
3. Bigler ED, Maxwell WL. Neuropathology of mild traumatic brain injury: Relationship to neuroimaging findings. Brain Imaging Behav 2012;6:108–36
4. Kim JJ, Gean AD. Imaging for the diagnosis and management of traumatic brain injury. Neurotherapeutics 2011;8:39–53
5. McAllister TW, Ford JC, Ji S, et al. Maximum principal strain and strain rate associated with concussion diagnosis correlates with changes in corpus callosum white matter indices. Ann Biomed Eng 2012;40:127–40
6. Smith DH, Hicks R, Povlishock JT. Therapy development for diffuse axonal injury. J Neurotrauma 2012;30:307–23
7. Metting Z, Cerliani L, Rodiger LA, et al. Pathophysiological concepts in mild traumatic brain injury: Diffusion tensor imaging related to acute perfusion CT imaging. PLoS One 2012;8:e64461
8. Hellyer PJ, Leech R, Ham TE, et al. Individual prediction of white matter injury following traumatic brain injury. Ann Neurol 2013;73:489–99
9. Niogi SN, Mukherjee P. Diffusion tensor imaging of mild traumatic brain injury. J Head Trauma Rehabil 2010;25:241–55
10. McMahon PJ, Hricik AJ, Yue JK, et al. Symptomatology and functional outcome in mild traumatic brain injury: Results from the prospective TRACK-TBI Study. [August 17, 2013 ePub ahead of print] J Neurotrauma
11. Lotocki G, de Rivero Vaccari J, Alonso O, et al. Oligodendrocyte vulnerability following traumatic brain injury in rats. Neurosci Lett 2011;499:143–8
12. Shaw K, MacKinnon MA, Raghupathi R, et al. TUNEL-positive staining in white and grey matter after fatal head injury in man. Clin Neuropathol 2001;20:106–12
13. Powers BE, Sellers DL, Lovelett EA, et al. Remyelination reporter reveals prolonged refinement of spontaneously regenerated myelin. Proc Natl Acad Sci U S A 2013;110:4075–80
14. Murtie JC, Zhou YX, Le TQ, et al. PDGF and FGF2 pathways regulate distinct oligodendrocyte lineage responses in experimental demyelination with spontaneous remyelination. Neurobiol Dis 2005;19:171–82
15. Nait-Oumesmar B, Picard-Riera N, Kerninon C, et al. Activation of the subventricular zone in multiple sclerosis: Evidence for early glial progenitors. Proc Natl Acad Sci U S A 2007;104:4694–9
16. Rasmussen S, Imitola J, Ayuso-Sacido A, et al. Reversible neural stem cell niche dysfunction in a model of multiple sclerosis. Ann Neurol 2011;69:878–91
17. Gallo V, Armstrong RC. Myelin repair strategies: A cellular view. Curr Opin Neurol 2008;21:278–83
18. Clarner T, Diederichs F, Berger K, et al. Myelin debris regulates inflammatory responses in an experimental demyelination animal model and multiple sclerosis lesions. Glia 2012;60:1468–80
19. Johnson VE, Stewart JE, Begbie FD, et al. Inflammation and white matter degeneration persist for years after a single traumatic brain injury. Brain 2013;136:28–42
20. White RE, Rao M, Gensel JC, et al. Transforming growth factor alpha transforms astrocytes to a growth-supportive phenotype after spinal cord injury. J Neurosci 2011;31:15173–87
21. Creed JA, DiLeonardi AM, Fox DP, et al. Concussive brain trauma in the mouse results in acute cognitive deficits and sustained impairment of axonal function. J Neurotrauma 2011;28:547–63
22. Kuo LW, Chen JH, Wedeen VJ, et al. Optimization of diffusion spectrum imaging and q-ball imaging on clinical MRI system. Neuroimage 2008;41:7–18
23. Wang Y, Wang Q, Haldar JP, et al. Quantification of increased cellularity during inflammatory demyelination. Brain 2011;134:3590–3601
24. Wedeen VJ, Hagmann P, Tseng WY, et al. Mapping complex tissue architecture with diffusion spectrum magnetic resonance imaging. Magn Reson Med 2005;54:1377–86
25. Sun SW, Liang HF, Trinkaus K, et al. Noninvasive detection of cuprizone induced axonal damage and demyelination in the mouse corpus callosum. Magn Reson Med 2006;55:302–8
26. Xie M, Tobin JE, Budde MD, et al. Rostrocaudal analysis of corpus callosum demyelination and axon damage across disease stages refines diffusion tensor imaging correlations with pathological features. J Neuropathol Exp Neurol 2010;69:704–16
27. Pierpaoli C, Walker L, Irfanoglu MO, et al. TORTOISE: An integrated software package for processing of diffusion MRI data, ISMRM, 18th Annual Meeting. 2010, 1597
28. Armstrong RC, Le TQ, Frost EE, et al. Absence of fibroblast growth factor 2 promotes oligodendroglial repopulation of demyelinated white matter. J Neurosci 2002;22:8574–85
29. Armstrong RC, Le TQ, Flint NC, et al. Endogenous cell repair of chronic demyelination. J Neuropathol Exp Neurol 2006;65:245–56
30. Johnson VE, Stewart W, Smith DH. Axonal pathology in traumatic brain injury. Exp Neurol 2013;246:35–43
31. Zakaria N, Kallakuri S, Bandaru S, et al. Temporal assessment of traumatic axonal injury in the rat corpus callosum and optic chiasm. Brain Res 2012;1467:81–90
32. Doerflinger NH, Macklin WB, Popko B. Inducible site-specific recombination in myelinating cells. Genesis 2003;35:63–72

33. Badea TC, Hua ZL, Smallwood PM, et al. New mouse lines for the analysis of neuronal morphology using CreER(T)/loxP-directed sparse labeling. PLoS One 2009;4:e7859

34. Zhou YX, Pannu R, Le TQ, et al. Fibroblast growth factor 1 (FGFR1) modulation regulates repair capacity of oligodendrocyte progenitor cells following chronic demyelination. Neurobiol Dis 2012;45:196–205

35. Sturrock RR. Myelination of the mouse corpus callosum. Neuropathol Appl Neurobiol 1980;6:415–20

36. Zhao Z, Loane DJ, Murray MG 2nd, et al. Comparing the predictive value of multiple cognitive, affective, and motor tasks after rodent traumatic brain injury. J Neurotrauma 2012;29:2475–89

37. Reeves TM, Phillips LL, Povlishock JT. Myelinated and unmyelinated axons of the corpus callosum differ in vulnerability and functional recovery following traumatic brain injury. Exp Neurol 2005;196:126–37

38. Sofroniew MV, Vinters HV. Astrocytes: Biology and pathology. Acta Neuropathol 2010;119:7–35

39. Lindner M, Heine S, Haastert K, et al. Sequential myelin protein expression during remyelination reveals fast and efficient repair after central nervous system demyelination. Neuropathol Appl Neurobiol 2008;34:105–14

40. Mason JL, Langaman C, Morell P, et al. Episodic demyelination and subsequent remyelination within the murine central nervous system: Changes in axonal calibre. Neuropathol Appl Neurobiol 2007;27:50–8

41. Wu C, Orringer DA, Lau D, et al. Cumulative incidence and predictors of neurosurgical interventions following nonsevere traumatic brain injury with mildly abnormal head imaging findings. J Trauma Acute Care Surg 2012;73:1247–53

42. Bennett RE, Mac Donald CL, Brody DL. Diffusion tensor imaging detects axonal injury in a mouse model of repetitive closed-skull traumatic brain injury. Neurosci Lett 2012;513:160–5

43. Song SK, Yoshino J, Le TQ, et al. Demyelination increases radial diffusivity in corpus callosum of mouse brain. Neuroimage 2005;26:132–40

44. Stone JR, Singleton RH, Povlishock JT. Antibodies to the C-terminus of the beta-amyloid precursor protein (APP): A site specific marker for the detection of traumatic axonal injury. Brain Res 2000;871:288–302

45. DiLeonardi AM, Huh JW, Raghupathi R. Impaired axonal transport and neurofilament compaction occur in separate populations of injured axons following diffuse brain injury in the immature rat. Brain Res 2009;1263:174–82

46. Dileonardi AM, Huh JW, Raghupathi R. Differential effects of FK506 on structural and functional axonal deficits after diffuse brain injury in the immature rat. J Neuropathol Exp Neurol 2012;71:959–72

47. Tobin, JE, Xie M, Le TQ, et al. Reduced axonopathy and enhanced remyelination after chronic demyelination in fibroblast growth factor 2 (fgf2)-null mice: Differential detection with diffusion tensor imaging. J Neuropathol Exp Neurol 2011;70:157–65

48. Tang-Schomer MD, Johnson VE, Baas PW, et al. Partial interruption of axonal transport due to microtubule breakage accounts for the formation of periodic varicosities after traumatic axonal injury. Exp Neurol 2012;233:364–72

49. Kumar A, Stoica BA, Sabirzhanov B, et al. Traumatic brain injury in aged animals increases lesion size and chronically alters microglial/macrophage classical and alternative activation states. Neurobiol Aging 2013;34:1397–411

50. Shitaka Y, Tran HT, Bennett RE, et al. Repetitive closed-skull traumatic brain injury in mice causes persistent multifocal axonal injury and microglial reactivity. J Neuropathol Exp Neurol 2011;70:551–67

51. Smith C, Gentleman SM, Leclercq PD, et al. The neuroinflammatory response in humans after traumatic brain injury. Neuropathol Appl Neurobiol 2013;39:654–66

52. Wilson S, Raghupathi R, Saatman KE, et al. Continued in situ DNA fragmentation of microglia/macrophages in white matter weeks and months after traumatic brain injury. J Neurotrauma 2004;21:239–50

53. Flygt J, Djupsjo A, Lenne F, et al. Myelin loss and oligodendrocyte pathology in white matter tracts following traumatic brain injury in the rat. Eur J Neurosci 2013;38:2153–65

54. Gensert JM, Goldman JE. Endogenous progenitors remyelinate demyelinated axons in the adult CNS. Neuron 1997;19;197–203

55. Aguirre A, Dupree JL, Mangin JM, et al. A functional role for EGFR signaling in myelination and remyelination. Nat Neurosci 2007;10:990–1002

56. Chen XH, Iwata A, Nonaka M, et al. Neurogenesis and glial proliferation persist for at least one year in the subventricular zone following brain trauma in rats. J Neurotrauma 2003;20:623–31

57. Chen S, Pickard JD, Harris NG. Time course of cellular pathology after controlled cortical impact injury. Exp Neurol 2003;182:87–102

58. Simons M, Snaidero N, Aggarwal S. Cell polarity in myelinating glia: From membrane flow to diffusion barriers. Biochim Biophys Acta 2012;1821:1146–53

59. Peters A. The effects of normal aging on myelin and nerve fibers: A review. J Neurocytol 2002;31:581–93

60. Rosenbluth J. Redundant myelin sheaths and other ultrastructural features of the toad cerebellum. J Cell Biol 1966;28:73–93